Contributions to Mineralogy and Petrology (2025) 180:23
https://doi.org/10.1007/s00410-025-02209-5

ORIGINAL PAPER

Exploring microstructures and anisotropies of serpentinites

Hans-Rudolf Wenk[1] · Amartya Kattemalavadi[1] · Yiming Zhang[1] · Ellis R. Kennedy[2] · Olaf Borkiewicz[3]

Received: 17 October 2024 / Accepted: 31 January 2025

Abstract
Serpentine minerals have received a lot of attention because of their unique crystal structures, their wide occurrence in orogenic belts and their potential role in contributing seismic anisotropy in subducting slabs. Several studies have investigated crystal preferred orientation (CPO) in high temperature antigorite serpentinites from Japan, the Alps, Spain, Cuba and Tibet, documenting significant crystal alignment. However, only a limited number of lower grade serpentines have been explored to date. Mainly because of submicroscopic microstructural heterogeneities CPO cannot be measured with conventional methods such as optical microscopy and EBSD. In this study 15 serpentinites from different tectonic settings in California, the Central Alps and Northern Spain have been investigated, mainly with high energy synchrotron X-ray diffraction, to quantify bulk crystal alignment. We find that CPO is strong on sheared surfaces of fractured blocks and secondary veins but the bulk of most serpentinite samples, except high-grade recrystallized antigorite serpentinite, show only weak crystal alignment. Correspondingly calculated seismic anisotropy based on CPO is not very significant. This is supported by very heterogeneous microstructures as documented with SEM and TEM analyses.

Keywords Serpentinite · Seismic anisotropy · Microstructures · Crystal preferred orientation

Introduction

Serpentinite is a rock that has received considerable attention including a book (O'Hanley 1996) and many publications on various topics. It occurs all over the world in different tectonic settings. Serpentinite is a complex system, often heterogeneous at all scales as highlighted by Evans et al. (2013): "Serpentine: What, Why, Where?".

Serpentinite rocks are composed mainly of the mineral serpentine and form as a result of transformation of mafic and ultramafic rocks along mid-oceanic ridges (e.g. Boschi et al. 2013; Kelley et al. 2005; Kuehn et al. 2021; Schroeder et al. 2002) and are an important rock type along passive continental margins (e.g. Debret et al. 2024), They also occur in subduction zones (e.g. Coleman 1971; Long and Becker 2010) or contact metamorphism of ultramafic rocks (e.g. Springer 1974).

Serpentine is a sheet silicate with a chemical composition $(Mg,Fe)_3[Si_2O_5](OH)_4$. There are three prevalent polymorphs, antigorite, lizardite and chrysotile as well as polyhedral polysomes. Pressure–temperature phase diagrams have been proposed (e.g. Day et al. 1985; Hilairet et al. 2006; Schwartz et al. 2013). It is generally recognized that antigorite occurs at higher metamorphic grade than lizardite (e.g. Caruso and Chernosky 1979; Evans et al. 1976; Laurora et al. 2011; Moody 1976; Nestola et al. 2010; O'Hanley et al. 1989) and chrysotile forms at low pressure conditions (e.g. Cogulu and Laurent 1984; Evans 2004; Hemley et al. 1977; Viti and Mellini 1997). But serpentine may not crystallize in thermodynamic equilibrium (e.g. Evans 2010) and the polymorph that forms is influenced by many factors, including local water pressure, Al-content, Fe-content, local instabilities and silica activity (e.g. Bromiley and Pawley 2003; Chernosky et al. 1988; Frost and Beard 2007; Tarling et al. 2019) and variable iron oxidation states (e.g. Andreani et al. 2007, 2013). Often there are

Communicated by Othmar Müntener.

✉ Hans-Rudolf Wenk
wenk@berkeley.edu

[1] Department of Earth and Planetary Science, University of California, Berkeley, CA 74720-4767, USA

[2] Department of Materials Science and Engineering, University of California Berkeley, Berkeley, CA 94720, USA

[3] Advanced Photon Source, Argonne National Laboratory, Lemont, IL 60439, USA

Published online: 03 March 2025

intergrowths of polymorphs at the atomic scale, even of chlorite and serpentine (e.g. Zhang et al. 2021).

Serpentinites are significant for tectonic processes (e.g. Guillot et al. 2015; Hermann et al. 1997, 2000; Wang et al. 2013). Even though they generally occur in small volumes, they lubricate shear zones, including the San Andreas fault and Melones fault in California (e.g. Melosh 2019; Moore and Rymer 2007). They act as wedges above descending slabs in subduction zones (e.g. Jung 2011; Zhao et al. 2020) and plate bending could play an important role (e.g. Ranero and Pérez-Gussinyé 2010). Mechanical properties have been explored with experiments to address plasticity, documenting low viscosity of serpentinites (e.g. Burdette and Hirth 2022; Escartín et al. 1997; Hilairet et al. 2007; Raleigh and Paterson 1965).

At low temperatures frictional sliding causes strengthening and, on the microscopic scale, introduces stacking faults, shear bands and kinks (e.g. Amiguet et al. 2014; Chernak and Hirth 2010; Jung and Green 2004; Jung et al. 2009). Other experiments focused on dehydration in subduction zones (e.g. Hirose et al. 2006; Ulmer and Trommsdorff 1995; Jung et al. 2009; Padrón-Navarta et al. 2010). Serpentine has recently gained interest as potential source of hydrogen produced by degassing (e.g. Lefeuvre et al. 2021; Truche et al. 2024) and the significance as a sink of organic and inorganic carbon (e.g. Bouilhol et al. 2022).

However, most attention on serpentine has been focused on its contribution to seismic anisotropy, with at least 30 publicatons sharing "serpentinite" and "anisotropy" in the title (among them are Bezacier et al. 2010; Deng et al. 2022; Ji et al. 2013; Jung 2011; Liu et al. 2020; Park et al. 2004; Schmitt et al. 2007; Shao et al. 2014; Watanabe et al. 2014). Seismic anisotropy is often linked to crystal preferred orientation (CPO) of minerals and single crystals of serpentine are indeed elastically strongly anisotropic based on first principles calculations, assuming ideal crystals (e.g. Satta et al. 2022; Deng et al. 2022). Serpentinite likely contributes to observed seismic anisotropy in subduction zones (e.g. Christensen 2004; Díaz et al. 2006; Guillot et al. 2004; Ji et al. 2013; Katayama et al. 2009; Long and Becker 2010; Michibayashi and Mainprice 2004; Park et al. 2004; Wiens et al. 2008; Yamasaki and Seno 2003) but as we will document it may not be a primary factor.

There are relatively few reports on CPO of serpentinite. Most studies are on high-grade antigorite-serpentinites with recrystallized fabrics and large grains which can be investigated with optical microscopy and electron backscatter diffraction (EBSD). Examples are from Japan (Hirauchi et al. 2010a, b; Nagaya et al. 2017; Nishii et al. 2011; Soda and Takagi 2010; Soda and Wenk 2014; Watanabe et al. 2011, 2014), Cuba (Auzende et al. 2002; Bezacier et al. 2010; Van de Moortele et al. 2010), Guatemala (Brownlee et al. 2013), the Betic Cordillera in Southern Spain (Padrón-Navarta et al. 2012; Dilissen et al. 2018), Valmalenco in the Southern Alps (Clément et al. 2019; Jung 2011; Kern et al. 1997, 2015; Liu et al. 2020; Morales et al. 2018) and Tibet (Shao et al. 2014). Recently, Kuehn et al. (2021) investigated CPO of lizardite in serpentinite from the Mid-Atlantic Ridge with synchrotron X-ray methods similar to those used in this study and documented very weak CPO.

Here we are following up by investigating crystal alignment and elastic anisotropy in 15 samples from different tectonic settings in California, the Central Alps and Northern Spain. Emphasis is on quantifying CPO and corresponding elastic anisotropy, not on relating it to the geologic environment.

Serpentine crystal structures

The mineral serpentine (nominal chemical formula $Mg_3[Si_2O_5](OH)_4$ is a single layer phyllosilicate with stacks of tetrahedral–octahedral sheets (Fig. 1, e.g. Brigatti et al. 2013). Tetrahedra are mostly $[SiO_4]$ and octahedra $[Mg(O,OH)_6]$, and some oxygens are shared. Contrary to sheet silicates like talc and chlorite which have silica layers on both sides of the octahedral layer, in serpentine there is only a single tetrahedral layer. This configuration introduces distortions due to slight differences in oxygen–oxygen bonds between the tetrahedral and octahedral layers. Unlike double-layer sheet silicates, where tetrahedral layers balance on either side of the octahedral layer, the single-layer structure of serpentine leads to bending, as depicted in Fig. 1c, d.

The ideal layered structure of serpentine with no bending is *lizardite* (e.g. Laurora et al. 2011; Mellini 1982; Mellini et al. 1987; Mellini and Zanazzi 1987; Mellini and Viti 1994) with a layer spacing ~ 7.3 Å. Bending gives rise to polymorphs such as *chrysotile* with curling to form fibrous structures (Fig. 1c, e.g. Falini et al. 2004; Pollastri et al. 2016) or periodic switching of tetrahedral layers as in *antigorite* (Fig. 1d, e.g. Capitani and Mellini 2004, 2006). A modification of chrysotile is the *polygonal structure*, also fibrous but divided into curved segments (e.g. Baronnet and Devouard 1996; Tarling et al. 2021). Another form is the 3D onion-like *polyhedral structure* (e.g. Andreani et al. 2008). In chrysotile fibers are along the [100] direction, vertical in Fig. 1a (e.g. Jagodzinski and Kunze 1954; Whittaker 1956). The antigorite polysome with $m = 17$ tetrahedra spanning over the wavelength and a corresponding $b = 43.7$ Å lattice parameter is used in this study (Capitani and Mellini 2006). There are other antigorite polysomes with m ranging from 13 to 23 (e.g. Capitani et al. 2009; Uehara and Shirozu 1985). Symmetry and lattice parameters of the main

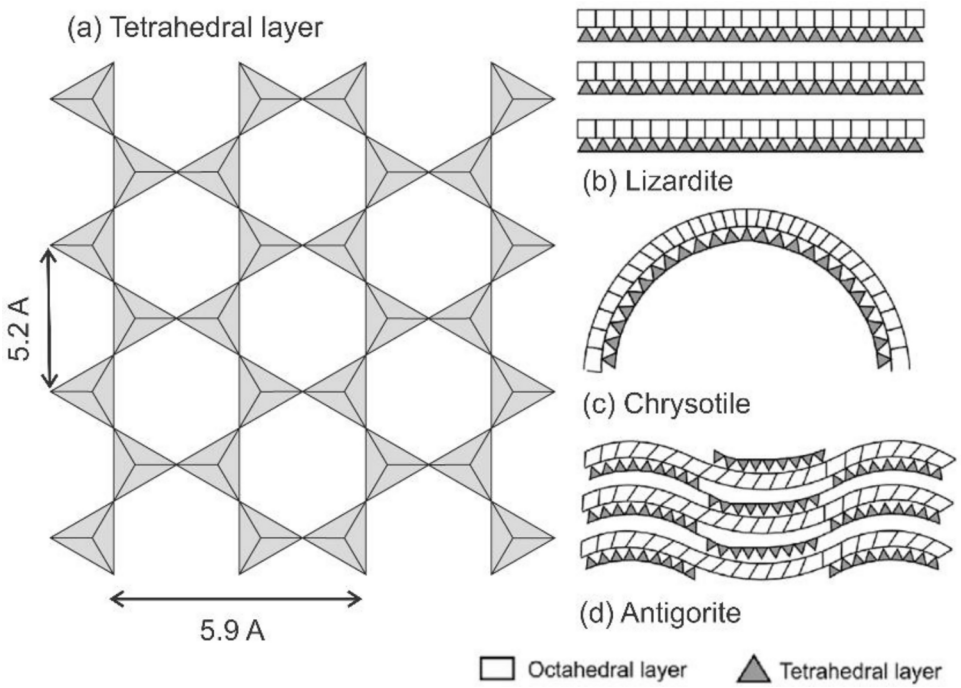

Fig. 1 Information about crystal structures of serpentine polymorphs. **a** Illustrates a layer of silicon tetrahedra. 5.2 Å corresponds to the repeat of tetrahedra along tetrahedral chains in the vertical direction and 5.9 Å along the horizontal direction. **b** The stacking of tetrahedral/octahedral layers in lizardite. **c** In chrysotile the layers curl to form tubes. **d** In antigorite the layers switch periodically to minimize stress

Table 1 Crystallographic information about minerals used in this study, amscd refers to the American Mineralogist Crystal Structure Database for crystal information files (cif) used in the Rietveld refinement

Mineral	Space group	Lattice parameters (Å, °) (*a, b, c, α, β, γ*)	amcsd code	Authors
Serpentine polymorphs				
Antigorite	Pm	43.505 9.251 <u>7.263</u> 90 91.32 90	3192	Capitani and Mellini (2004)
Lizardite	P31m	5.323 5.3234 <u>7.272</u> 90 90 120	18,972	Laurora et al. (2011)
Chrysotile	Cc	5.340 9.241 <u>14.69</u> 90 93.66 90	19,917	Falini et al. (2004)
Others				
Chlorite	C2/m	5.336 9.240 14.37 90 96.93 90	4284	Zanazzi et al. (2007)
Andradite	Ia-3d	12.031 12.031 12.031 90 90 90	1207	Hazen and Finger (1989)
Magnetite	Fd-3m	8.395 8.395 8.395 90 90 90	9109	Gatta et al. (2007)

The layer spacing is underlined. For monoclinic crystals the second setting convention is displayed, in the Rietveld refinement the first setting is used (Matthies and Wenk 2009)

three serpentine polymorphs as well as for other minerals used in this study are listed in Table 1. References also refer to crystal information files (cif) used in the refinement of X-ray diffraction data. Note that for trigonal lizardite the layer spacing is along the crystallographic *c-axis*, and *a* corresponds to the spacing along tetrahedral chains (Fig. 1a, vertical). Antigorite and chrysotile are monoclinic which causes some complexities for texture analysis which will be explained later. In Fig. 1 and Table 1 the second setting with γ as angle between a and b axes is used.

Samples

This section gives a brief overview of the tectonic settings of the samples investigated in this study. They were selected from our serpentinite collection from different localities in California, the Central Alps and Northern Spain to provide an overall picture of variations in microstructures and particularly crystal preferred orientation (CPO) that is significant for predicting seismic anisotropy. We are not going to relate those properties to local geological features such as subduction zones and shear faults or explore variations at the outcrop scale.

Samples are listed in Table 2 (for exact location on a map enter coordinates on Google Earth) and Supplementary Fig. 1a–c provides overviews of sample locations in a geological context. Snapshots of hand specimens and some outcrops are displayed in Fig. 2 and Fig. 4a (Brg758). Surfaces of hand specimens are often glossy, with striations (e.g. Fig. 2j), however the interiors are generally dark and appear homogeneous (Fig. 2j, right side). Sometimes there are multiple generations of crosscutting veins (Fig. 2e, n). Most samples studied are bulk material but we also explored some layers of fibrous aggregates on fracture surfaces (NS11, SN100, Brg1852 and Her1).

Table 2 Sample name, sample location, coordinates, estimated composition and accessories (act: actinolite, and: andradite, ant: antigorite, chl: chlorite, chr: chromite, chrys: chrysotile, liz: lizardite, mag: magnetite, mil: millerite, oli: olivine, pent: pentlandite)

Sample	Location	Coordinates N/EW	Composition volume fraction%	Accessories
California				
NS10 bulk	Yuba River	39°54′11″N 121°21′07″W	ant63 chl29 mag8	talc
NS11 surface	Yuba River	39°54′11″N 121°21′07″W	ant17 chl7 and76	pent mag act
SN100 fibrous	Forestville	38°59′03″N 120°50′24″W	ant100	
MW1 bulk	Muir Beach	37°52′30″N 122°35′54″W	ant57 chl43	
SBen2 bulk	San Benito	36°23′24″N 120°39′24″W	liz100	
SBen2 vein	San Benito	36°23′24″N 120°39′24″W	liz100	chrys
Central Alps				
Brg758 vein	Mungiroi	46°23′48″N 9°34′10″E	ant100	
Brg1851 bulk	Grevasalvas	46°25′37″N 9°42′24″E	liz100	mil mag
Brg1852fibrous	Grevasalvas	46°25′37″N 9°42′24″E	chrys100	mag
Brg1863 bulk	Plaun da Lei	46°25′07″N 9°43′24″E	liz51 chl23 mag26	dolomite titanite
Brg1870 bulk	Marmorera	46°30′48″N 9°37′54″E	liz100	chr
K987 bulk	Valmalenco	46°15′26″N 9°51′03″E	ant98 oli2	diopside mil
Spain				
Ca11 bulk	Moeche	43°32′37″N 7°59′38″W	ant100	chr pent
Ca14 bulk	Moeche	43°32′37″N 7°59′38″W	ant58 chl42	chr mil talc
Ca16 bulk	Moeche	43°32′37″N 7°59′38″W	ant99 mag1	chr
Her1 fibrous	Herbeira	43°43′19″N 7°56′47″W	ant100	

Enter coordinates into "Search" on Google Earth and it will show you exact location on a map. The volume fractions were obtained from the Rietveld refinement. Minor mineral phases were mainly identified with energy dispersive spectroscopy

California

There are outcrops of serpentinite in many parts of California, and it has earned the reputation of "California State Rock" (e.g. Rakovan 2011). An elongated zone of serpentinites is exposed along the Western Sierra Nevada Foothills metamorphic belt (Suppl. Fig. 1a). Compressional forces associated with accretionary growth of the western margin of the North America plate during Upper Paleozoic to Jurassic led to the accretion of dominantly ophiolite-chert-argillite rocks onto the continent at different intervals (ca. 300, 200, 160 Ma., Saleebe 1982). Metamorphism caused a partial alteration of mafic and ultramafic rocks into serpentinites that are now exposed (e.g. Andreani et al. 2005; Moores 1970; Springer 1974). Many serpentinite deposits are in vicinity of the north–south extending Bear Mountains and Melones faults in the Sierra Nervada foothills (Suppl. Fig. 1a). These faults were active in late Jurassic with an east over west dip-slip motion (e.g. Paterson and Wainger 1991). We investigated samples NS10 and 11 (mainly antigorite) along highway 70 near the Yuba River (Fig. 2a, b), and SN100 (chrysotile/antigorite intergrowth) near Forestville, CA (Fig. 2c).

The Franciscan Complex is a Cretaceous accretionary mélange containing blocks of graywacke, greenstone, blueschist, and serpentinized ophiolite (e.g. Ernst 1988, 2011; Wakabayashi 2017). The formation and metamorphism of the Franciscan ultramafic rocks occurred in association with subduction during the Jurassic to Cretaceous along the western North American margin. Thin accretionary wedges of ultramafic rocks were partially serpentinized, with many small outcrops such as Muir Woods, central San Francisco, Lake Berryessa and Mount Diablo in the Bay Area. They are locally associated with eclogites (e.g. Cisneros et al. 2022). Uplift of the present-day Coast Range in the Cenozoic and activity with the San Andreas fault system have led to the current surface exposures of serpentinite (e.g. Barnes et al. 2013; Montgomery 1993). Sample MW1 (antigorite/chlorite) was collected along California State Route 1 between Muir Beach and Stinson Beach (Fig. 2d).

One of the largest serpentinite blocks in California is near New Idria in San Benito County (e.g. Coleman 1971; Wakabayashi 2004, 2017). This region has attracted a lot of interest because of the large Coalinga asbestos mine (e.g. Cooper et al. 1979; Mumpton and Thompson 1975). Sample SBen2 (lizardite with chrysotile vein) was collected near San Benito Mountain northwest of Coalinga (Fig. 2e).

Central Alps

The Cretaceous to Tertiary Alpine orogeny involves the convergence of the African and European plates and the closure of the Tethys Ocean (e.g. Schmid et al. 2004). During the orogeny, parts of the Tethys oceanic lithosphere containing upper mantle gabbros, peridotites, serpentinites, ophicarbonates and metapelites were juxtaposed between Pennine nappes in the north at the bottom, belonging to the European crust, and the Austroalpine nappes in the southeast on top, from the African crust (e.g. Hermann et al. 1997, 2000, Supplementary Fig. 1b).

Ultramafic rocks occur in the Western Alps, such as the Zermatt-Saas zone, associated with high-pressure eclogites (e.g. Angiboust et al. 2009; Auzende et al. 2006b; Wassmann

Fig. 2 Serpentinite hand specimens and outcrops for some of the samples used in this study. **a** An outcrop at Yuba River; **b** corresponding sample NS10; **c** sample SN100 with a layer of fibrous chrysotile near Forestville CA; **d** sample MW1 near Muir Woods from California Coast Range; **e** SBen2 with ground mass crosscut by lighter chrysotile veins from San Benito Mountain; **f** Plaun Grand outcrop, above Grevasalvas in the Northern Bergell Alps, corresponding to Brg1851 (**g**), with homogeneous dark bulk matrix and polished surfaces and (**h**) Brg1852, a fibrous layer consisting of chrysotile; **i** Outcrop Plaun da Lei/Maloja with sample Brg1863 (bright vein is dolomite); **j** sample Brg1870 from Marmorera; **k** Herbeira quarry, N Spain; hand specimens Ca11 (**l**), Ca14 (**m**) and Ca16 (**n**) from Moeche. **o** Her1 fibrous layer of antigorite from Herbeira

et al. 2011), the Ivrea-zone with high-temperature serpentinites and peridotites at Finero with metasomatic processes (e.g. Cannao et al. 2022; Hartmann and Wedepohl 1993). In the Central Alps there is a relatively narrow W–E stretched Chiavenna zone with variable olivine–talc–chlorite–serpentinite schists (e.g. Schmutz 1976) and further east a south-north extending Valmalenco-Platta unit between Pennine and Austroalpine nappes. In the Eastern Alps serpentinites are documented in the Tauern Window (e.g. Gross et al. 2020; Schmid et al. 2013) as well as the Slovenian Alps (e.g. De Hoog et al. 2009). Many of these ultramafic rocks have undergone significant transformations and are heterogeneous. Investigations have mainly explored geochemistry (e.g. Barnes et al. 2014).

Here, with a focus on bulk anisotropy, we selected fairly homogeneous serpentinites from the Platta-Valmalenco zone juxtaposed between upper Pennine and lower Austroalpine nappes (Suppl. Fig. 1b). Several samples of lower

greenschist facies Platta nappe serpentinites in the north were investigated (e.g. Bernoulli and Weissert 2021; Burkhard and O'Neill 1988; Dietrich and Peters 1971). The dominant phase is lizardite (Brg1851, Fig. 2g, Brg1863, Fig. 2i, Brg1870, Fig. 2j), except for a serpentine vein in Brg758 (Fig. 5a) which is antigorite and Brg1852 (Fig. 2h) in a fracture surface which is chrysotile.

The serpentinites in Valmalenco have received a lot of attention in terms of geochemistry (e.g. Clément et al. 2019; Kempf et al. 2022; Müntener et al. 2010; Peretti et al. 1992), tectonic-metamorphic history (e.g.Lafay et al. 2022; Müntener and Hermann 1996; Trommsdorff and Evans 1972) and mineralogy (e.g. Amthauer et al. 1974; Capitani and Mellini 2004; Mellini et al. 1987; Müntener and Hermann 1994; Zucali et al. 2018). They are of amphibolite facies metamorphic grade and the main polymorph is antigorite, with minor fractions of olivine and clinopyroxene. In the contact region with the Tertiary Bergell tonalite in the West, serpentinite has undergone metamorphic transformations to olivine and talc (Müntener et al. 2000; Trommsdorff and Evans 1972; Worden et al. 1991). The Valmalenco serpentinite was mined in several large quarries as decorative stone. Antigorite in the regularly foliated serpentinites displays high preferred orientation (e.g. Jung 2011; Kern et al. 1997, 2015; Morales et al. 2018), although there are local heterogeneities (Liu et al. 2020). Our sample K987 is antigorite from the Chiesa quarry of Nuova Serpentino d'Italia.

Northern Spain

A third sample locality is from Galicia in the Variscan orogenic belt in Northern Spain (Suppl. Fig. 1c). The Variscan belt of the Iberian Massif is the result of the Paleozoic Variscan orogeny which involves the collision between ancient continents Laurussia and Gondwana (e.g. Albert et al. 2012; Díez Fernández et al. 2011). The geology of the Iberian Massif is characterized by an autochthonous Gondwanan domain overlain by an allochthon, which consists of peri-Gondwanan terranes and ophiolites (Sánchez Martínez et al. 2007). The ophiolites that compose the middle part of northwestern Iberia are interpreted to be relics of the eastern branch of the Rheic Ocean which were subjected to greenschist to amphibolite facies metamorphism. Near Cabo Ortegal a Devonian event produced high temperature-high pressure metamorphism with eclogites (e.g. Girardeau et al. 1989; Ordóñez Casado et al. 2001). There are serpentinite quarries at Moeche and Cabo Ortegal (e.g. Nespereira et al. 2019). We report on serpentinite from the lower Moeche unit which is underneath the high-pressure allochthonous Cabo Ortegal complex (samples Ca11, 14, 16, Fig. 2l–n). The Moeche unit is in the center of a synclinal structure. One sample is from Herbeira (Her1, Fig. 2o) near Cabo Ortegal and was used for transmission electron microscopy characterization. All samples are dominantly antigorite.

Contrary to serpentinites in Galicia with very weak CPO, high pressure–temperature antigorite serpentinites with high Al-content (3.5–4 wt% Al_2O_3) from Cerro del Amirez in Southern Spain display strong preferred orientation as documented with EBSD measurements (Padrón-Navarta et al. 2012).

Analytical methods

The main goal of this study is to use crystal preferred orientation data to calculate elastic and seismic properties of a suite of bulk serpentinite rock samples. In this section we describe our analytical methods. We first use polished thin sections (~30 µm) to explore the major mineral phases and their structures, starting with a petrographic microscope, followed by scanning electron microscopy to identify microstructures and estimate the chemical composition of serpentine and other minor mineral phases in each sample. We then conducted transmission electron microscopy on a few samples, on thin foils prepared by focused ion beam (FIB) cuts (10–500 nm) to explore the heterogeneity of serpentine polymorphism at fine scales. Subsequently, quantitative texture analysis of synchrotron X-ray diffraction data was applied to calculate crystal orientation distributions, elastic properties and seismic wave velocities of the bulk samples. We also conducted Raman spectroscopy on some samples, but results will be reported in a separate study and compared with data from the literature (e.g. Compagnoni et al. 2021; Kashima et al. 2022; Rinaudo et al. 2003; Rooney et al. 2018).

Scanning electron microscopy (SEM)

SEM investigations used polished but not carbon-coated thin sections in a Zeiss EVO scanning electron microscope in the Department of Earth and Planetary Science at the University of California, Berkeley, in low vacuum mode to avoid charging, with an accelerating voltage of 20 kV and a beam current of ~2 nA. We mainly used backscatter electron (BE) detectors for imaging where the brightness of each phase imaged is dominantly related to their respective average atomic number, making it easy to identify the main components in the samples which typically include serpentine (dark with gradients), chlorite (brighter grey) and magnetite (very bright) (cf. Figs. 7, 8).

Energy-dispersive X-ray spectroscopy (EDS) analyses with an EDAX-AMETEK detector and analytical software were used to estimate atomic element fractions of O, Mg, Al, Si, Fe, Ca and Cr for serpentine and accessories (Table

S1 of supplementary material and Table 3). EDS data reduction was performed using the EDAX Genesis software. For quantification we applied corrections based on standards with well-defined compositions.

Transmission electron microscopy (TEM)

The ways in which different serpentine minerals accommodate the misfit of tetrahedral and octahedral layers give rise to different polymorphs and cause defects. It was the study of Yada (1971) displaying the scroll-like structure of chrysotile at atomic resolution with a TEM that sparked a lot of interest to explore polytypism and defects in serpentine with high resolution transmission electron microscopy.

Here we used a Thermo Fisher Scios 2 SEM with a focused ion beam (FIB) aperture at the Materials Science Department of UC Berkeley to prepare lamellar TEM samples from small serpentinite rock chips. These samples were then carbon-coated to prevent charging and analyzed with a high-resolution scanning TEM (STEM) FEI TitanX operated at 200 kV at the Molecular Foundry of Lawrence Berkeley National Laboratory. TEM analyses were performed on samples SN100, SBen2, Brg1852, and Her1.

Table 3 Serpentine cation atomic fractions normalized to 5.0 based on EDS analyses assuming a formula $(Mg, Fe)_3(Si, Al)_2O_5(OH)_4$

Sample	Mg	Fe	Si	Al
California				
NS10 bulk	2.82	0.15	1.97	0.06
NS11surface *bright*	2.77	0.15	2.08	0.00
NS11 surface *dark*	2.84	0.11	2.05	0.00
SN100	2.77	0.11	1.97	0.03
MW1 *bright*	2.69	0.19	1.84	0.06
MW1 *dark*	2.76	0.09	1.99	0.03
SBen2 bulk	2.84	0.13	1.97	0.06
SBen2 vein *bright*	2.68	0.22	1.90	0.19
SBen2 vein *dark*	2.86	0.11	1.98	0.06
Central Alps				
Brg758	2.78	0.18	2.04	0.00
Brg1851 *bright*	2.86	0.12	1.95	0.08
Brg1851 *dark*	2.87	0.08	1.99	0.06
Brg1863	2.73	0.19	1.91	0.17
Brg1870 *bright*	2.75	0.24	1.95	0.06
Brg1870 *dark*	2.78	0.08	2.08	0.05
K987	2.86	0.10	2.00	0.04
Spain				
Ca11 *bright*	2.74	0.20	1.96	0.07
Ca11 *dark*	2.76	0.18	1.98	0.06
Ca14 *bright*	2.56	0.26	1.95	0.24
Ca14 *dark*	2.73	0.21	1.99	0.07
Ca16 bulk *bright*	2.78	0.16	1.98	0.08
Ca16 bulk *dark*	2.87	0.10	1.96	0.04
Ca16 surface *bright*	2.71	0.22	1.92	0.15
Ca16 surface *dark*	2.72	0.20	1.97	0.12
Her1 *bright*	2.70	0.20	2.10	0.00
Her1 *dark*	2.63	0.17	2.12	0.09

See also Suppl. Table S1. The "*dark*" and "*bright*" refer to spot analyses with different grey shades in BSE images (Figs. 7, 8a)

Synchrotron X-ray texture analysis

The main goal of this study was to quantitatively determine crystal preferred orientation (CPO). On fairly fine-grained serpentinites this can be achieved with high energy synchrotron X-ray diffraction on bulk samples. The method was recently applied and refined to measure preferred orientation in slates (Wenk et al. 2022). Prismatic blocks of $4 \times 4 \times 10$ mm size were cut with a diamond saw, with the long direction perpendicular to the cleavage plane. Then prism edges were ground manually to approach a cylinder shape. The cylinders were then mounted on a metal rod (Fig. 3a top left).

The synchrotron diffraction experiments were performed at the Advanced Photon Source of Argonne National Laboratory at the high energy beamline 11-ID-C. A schematic of the experiment is shown in Fig. 3a. An X-ray beam with a wavelength of 0.1173 Å (115 keV) and focused to a size of ~ 1 mm reaches the sample mounted on a goniometer head with a horizontal rotation axis (X, ϕ-rotation). The sample is aligned by tilting and translating on the goniometer head to align the sample axis horizontally and bring the center of the cylinder into the center of the beam. About 10 cm behind the sample the primary beam is captured. The diffraction patterns are recorded with a Perkin Elmer 2D image plate detector mounted ~ 195 cm from the sample.

These experiments were conducted over several years (2013–2022) and some details have changed, both with the experimental set-up and the software used for data processing. Therefore we do not provide access to old diffraction images but provide links to data from the recent measurements (see Data Availability statement at the end of the paper).

The experiment takes advantage of the high energy of X-rays, not only for good sample penetration but also for low diffraction angles (a range of 2Θ of 0.5–3.5° was used, corresponding to ~ 22–2 Å). Therefore, lattice planes of recorded diffractions are barely tilted relative to the incoming X-ray (Θ 0.25–1.75°), providing an excellent pole figure coverage. In the schematic Fig. 3a a much larger wavelength is assumed. Before measuring samples, the instrument geometry is calibrated with a LaB_6 standard (a = 4.156468 Å), refining sample-detector distance, exact detector orientation and beam shape (Caglioti function, Caglioti et al. 1958).

Samples were then measured with 11 images at φ 15° rotation intervals from 0° to 165°. During the exposure the sample was translated along the cylinder axis (X) 2–3 mm

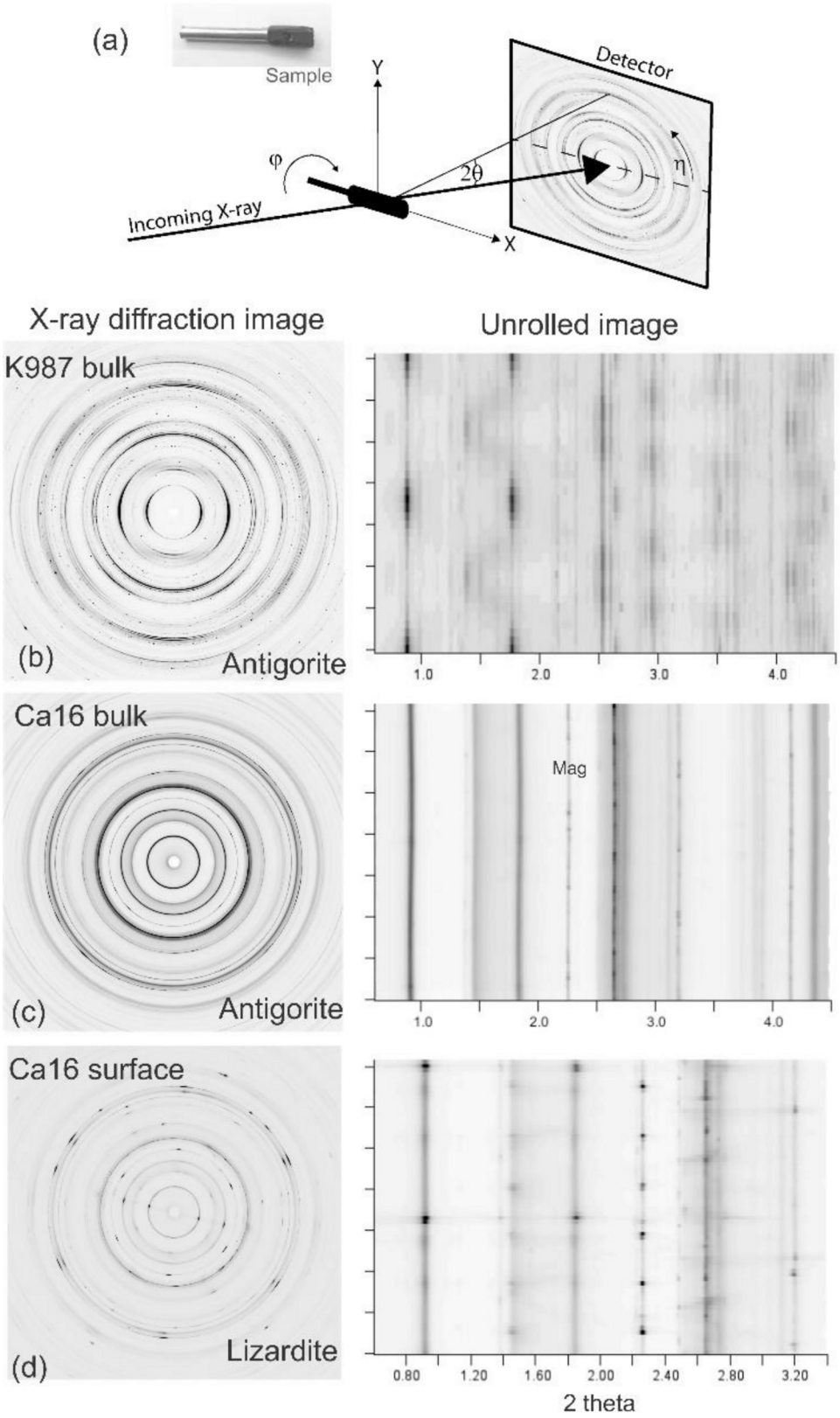

Fig. 3 **a** Schematic of synchrotron X-ray diffraction at APS beamline 11-ID-C. Cylindrical sample, 10 mm long and mounted on an aluminum rod (top left) is rotated around X (φ) perpendicular to the incident beam. 2Θ is exaggerated. In reality 2Θ is much smaller for high energy X-rays. Intensity variations along azimuth η are indicative of crystal preferred orientation. The diffraction image is antigorite K987. **b**–**d** Some typical X-ray diffraction images of serpentinites. Left side are actual diffraction images, right side are "unrolled" diffraction images with azimuth η vertical. **b** K987 from Valmalenco with very strong preferred orientation. **c** In Moeche serpentinite Ca16 from Northern Spain the bulk has almost no intensity variations but (**d**), on the surface displays very strong alignment, almost a single crystal superposed on the uniform background

to improve grain statistics. Each measurement, with mounting sample, software control, φ-rotations and exposure time, takes about 15 min. Some typical diffraction images are shown in Fig. 3b–d, left side. Azimuthal intensity variations indicate preferred orientation. This is even more apparent in Fig. 3b–d right side where images are "unrolled", and the vertical axis is azimuth η. It is immediately obvious that sample (b) has strong CPO, sample (c) has much weaker CPO and sample (d) from a fracture surface is almost a single crystal with distinct diffraction spots.

The 11 digital X-ray diffraction images at different rotations φ were then analyzed simultaneously with the Rietveld method (Rietveld 1969), which relies on a refinement with least-squares fit to minimize the difference between experimental diffraction data and a calculated model based on scattering background, crystal structures, volume fractions of components, crystal preferred orientation and grain size. For the Rietveld refinement the software MAUD version 2.98 was used (Lutterotti et al. 1997) and details are described in tutorials (e.g. Lutterotti et al. 2014).

First 2D images (Fig. 4) were integrated over 5° azimuthal sectors to produce 72 diffraction spectra. A total of $11 \times 72 = 792$ spectra were then used in the Rietveld refinement. A polynomial function with five coefficients was used to refine the background of each image in some of the samples and an interpolated background in others. The Rietveld refinement starts with model crystal structures and lattice parameters are subsequently refined. With serpentine polymorphism this can be rather complex as we will discuss below. As a start we use 43 Å monoclinic antigorite Pm, trigonal lizardite P31m, monoclinic chrysotile Cc, monoclinic chlorite C2/m, cubic andradite Ia-3d and cubic magnetite Dd-3m. The crystal information files (cif) were downloaded from the American Mineralogist Crystal Structure Database (amcsd). References for used cif files are given in Table 1. Note that for the texture analysis in MAUD of monoclinic crystals, such as antigorite, chrysotile and chlorite, the first setting needs to be applied, i.e. (100) is the cleavage plane instead of a more familiar second setting with (001) as the cleavage plane (Matthies and Wenk 2009). But for labels of lattice planes *hkl* in text, tables and figures we use in this paper the more conventional second setting, except for Supplementary Table 2. We have explored the accessory phase magnetite in some samples. It is expressed in sharp spot patterns in diffraction images and does not display CPO (e.g. Fig. 3c). In MAUD Advanced Models "arbitrary texture" was assumed for magnetite to refine the volume fraction. Some magnetite diffraction peaks were excluded from the image to minimize overlaps with diffraction peaks from serpentine minerals. Grain size and shape of components were refined using the Popa (1998) model.

The crystallographic preferred orientation distribution function (ODF) for each phase was refined with the EWIMV method (Matthies and Vinel 1982), not imposing any sample symmetry and with an ODF grid of 7.5°. The ODF was then exported from MAUD and imported into Beartex (Wenk et al. 1998), using the 2024 updated version, first to generate a binary ODF (with CMAU), smooth the ODF (with SMOO) and then to rotate the sample (with CSEC) such that the (001) maximum is in the center of the pole figure and, if there is a girdle-like distribution, the girdle is vertical. In a clearly foliated sample, such as Valmalenco antigorite K987, this would correspond to a projection on the foliation plane. In many serpentinites the foliation is not obvious, and the secondary rotation is done for easier comparison.

The transformed MAUD ODF's were then used to calculate pole figures (with PCAL) and plot pole figures (with PING) as well as generate average elastic properties (TENS and TENX) and calculate velocity pole figures (VELO). Orientation concentrations, both ODF and pole figures, are expressed in multiples of random distribution (mrd) with 1 mrd corresponding to an isotropic (random) distribution and ∞ to a single crystal. The strength of preferred orientation can also be expressed with the texture index ($J = \int f(g)^2 dg$, where f(g) is the 3D ODF; Bunge 1982, p. 88).

The method was tested in detail with sample Brg758 on prismatic crystals of serpentine growing in a vein of bulk serpentinite (Fig. 4a). Raman spectroscopy identified it as antigorite. A diffraction image (Fig. 4b) displays very strong preferred orientation with large intensity variations along Debye rings. We refined the sample's CPO from the same diffraction images but assuming different serpentine polymorphs. Figures 4c–e show data from one of 11 diffraction images that were used in the refinement. On the left side is an integration over azimuth η with black the measured spectrum and red the Rietveld fit. On the right side is a stack of diffraction spectra spread over azimuth η (vertical) with measured data at the bottom and top the calculated Rietveld fit. Intensity variations along the vertical axis η are indicative of CPO. It appears that the refinement assuming antigorite gives the best fit (Fig. 4c), but the calculated diffraction patterns of all three polymorphs are very similar, especially the fit for the main diffraction peaks which dominate the definition of the crystal orientations. Such similarities between the fits are also expressed in the pole figures (Fig. 5). In all three reconstructed sheet-plane normal (001) pole figures, there is a main maximum divided into a couple of sub-maxima. The direction of linked tetrahedra in serpentine (vertical in Fig. 1a) also agrees with the crystal structures. It is (010) for monoclinic antigorite and chrysotile, and (110) for trigonal lizardite. The CPO patterns are best described as two groups of hexagonal crystals that are slightly tilted with respect to

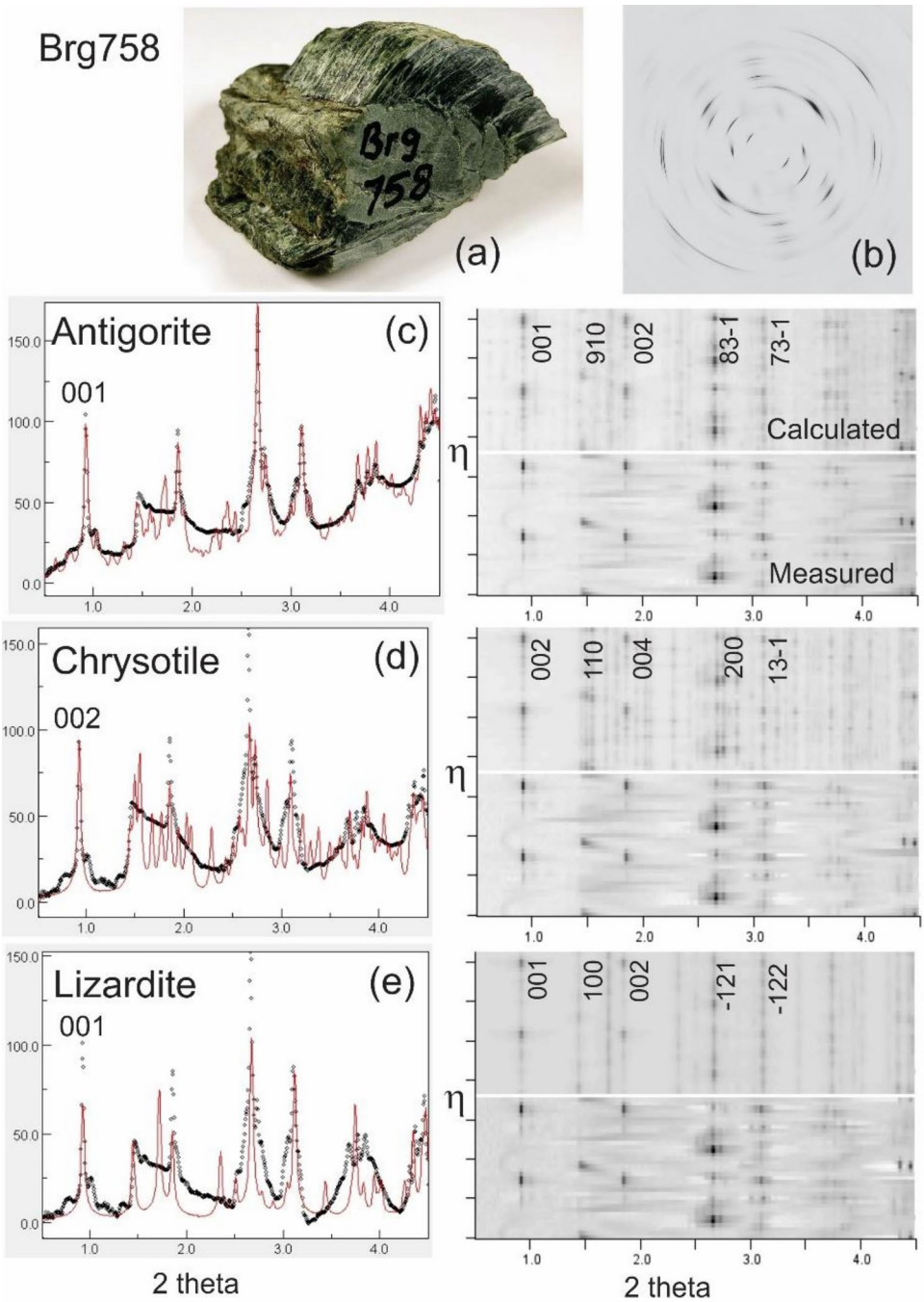

Fig. 4 **a** Hand specimen of serpentinite Brg758 from the Alps with a vein of highly aligned crystallites. **b** Select diffraction image displaying strong azimuthal intensity variations (η). **c**–**e** Modeling preferred orientation from the same diffraction images with MAUD using different serpentine polymorphs. Left column: Diffraction pattern obtained by azimuthal averaging over a selected image. Black is data, red is the Rietveld fit. Right column: Stack of 72 integrated 5° sectors stacked vertically. Bottom is measured data, top is Rietveld fit. (**c**) Model for antigorite, **d** chrysotile and **e** lizardite

each other. The hexagonal rotations would be expected for lizardite but they are also expressed in the monoclinic (010) and (100) pole figures for antigorite and chrysotile.

We will later show a case with (001) (sheet plane normals) rotating around $(100)_{mono}$ poles as one would expect for aligned chrysotile fibers and fibrous antigorite (cf. Fig. 12). Together, these results indicate that the quantification of serpentine preferred orientations is quite insensitive to the relatively minor diffraction planes in different types of serpentine polymorphs and gives us confidence that, using the crystal structure information for the dominant type of serpentine, one can reasonably reconstruct the CPO despite the fact that more than one type of serpentine polymorph may exist in a sample. In some ways it illustrates that texture analysis can be useful in exploring polymorphism since polymorphs basically repeat the same basic unit (lizardite, Fig. 1b) in different orientations.

Diffraction patterns of ideal serpentine structures (Fig. 1) are complex with many secondary peaks which are not expressed in observed patterns (Fig. 4; many red peaks in

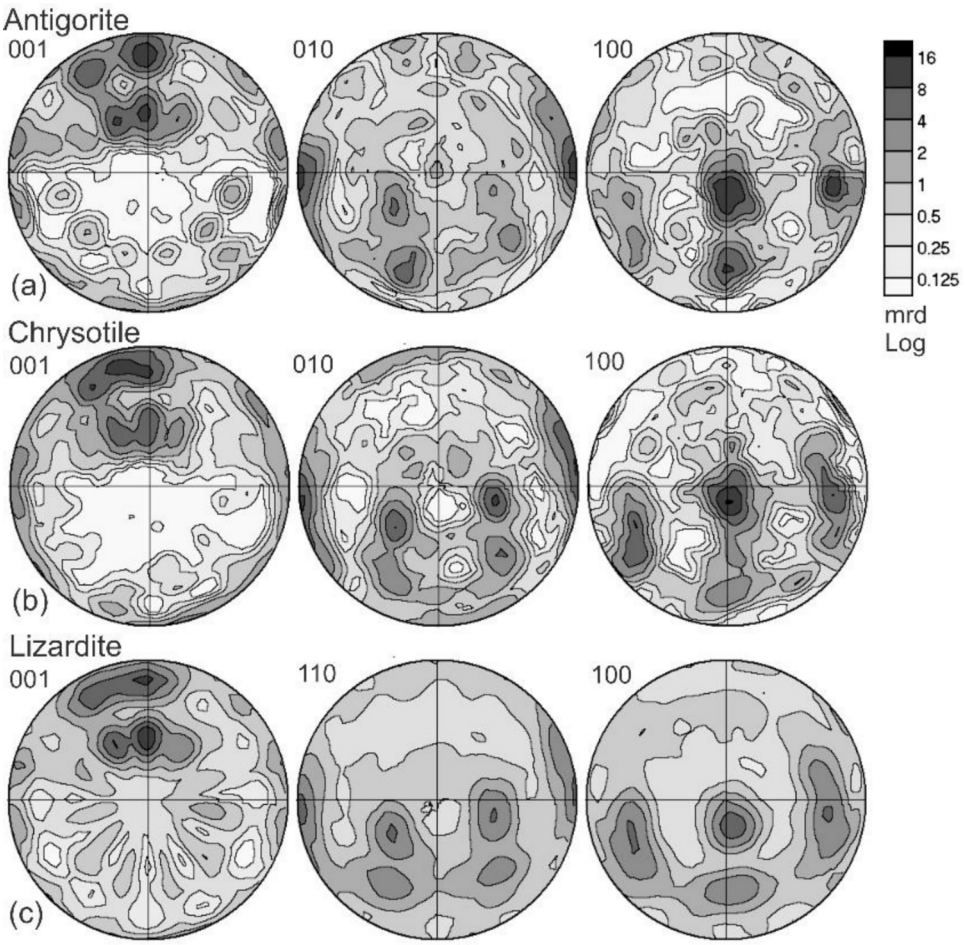

Fig. 5 Pole figures obtained for Brg758 by fitting the same measured synchrotron X-ray diffraction images assuming different serpentine polymorphs in MAUD; **a** antigorite, **b** chrysotile and **c** lizardite. Equal area projection, logarithmic pole density scale. Monoclinic pole figures (antigorite and chrysotile) use second setting for hkl symbols. The texture results are very similar for the different serpentine polymorph used. This indicates that MAUD textural fitting successfully captures the crystal preferred orientation patterns in the bulk sample, regardless of the relatively minor differences in the diffraction patterns of the different serpentine polymorphs

Rietveld fit do not match with the black measured diffraction pattern). This is due to defects such as stacking faults which are ubiquitous as will be documented with TEM images (Fig. 9). This complexity can be addressed in MAUD with a "Planar defects model" such as "Ufer single layer" which was applied to turbostratically disordered montmorillonite (Lutterotti et al. 2010). We applied it to some samples but effects on crystal preferred orientation are minimal because it relies on the main diffraction peaks.

Results and interpretations

Optical microscopy

Thin sections of samples, approximately 30 µm in thickness, were analyzed with a Nikon Optiphot-Pol petrographic microscope in transmission and cross-polarized light. Most were cut perpendicular to the visible foliation, though it is often not very well defined. A few examples are shown in Fig. 6 to illustrate characteristic features. NS10 (Fig. 6a) consists dominantly of serpentine that displays a mesh structure with gradients, somewhat reminiscent of the type described by Francis (1956) in Scottish serpentinites. The mesh size is 50–100 µm with distinct zoning. SN100 (Fig. 6b) is a slightly thicker section (higher interference colors) of a fibrous layer (Fig. 2c), with long fibers strongly aligned. SBen2 from San Benito (Fig. 6c) shows a 1.5 mm serpentine vein with highly aligned crystallites perpendicular to the contact between the vein and the matrix. Subsequent analyses reveal that the vein consists of chrysotile/polygonal serpentine. The serpentine matrix is very fine-grained lizardite (5–10 µm) with no obvious preferred orientation. Brg1852 (Fig. 6d) is also from a layer of fibrous aligned crystals (Fig. 2h) which were later identified as chrysotile. In Brg1863 (Fig. 6e) lizardite has a fairly uniform microstructure with poorly aligned grains, 5–20 µm in size. This is similar to the "interpenetrating texture" described by Wicks and Whittaker (1977) for low-temperature serpentinization of olivine. Figure 6f shows a low magnification image of Brg1870, composed mainly of lizardite with blocky regions divided into subgrains and more or less diagonally aligned crystallites. There is also a secondary vein of chrysotile. K987 (Fig. 6g) is serpentinite from Valmalenco (e.g. Kern et al. 2015) with strongly aligned antigorite platelets (grey–white) and some fairly equiaxed olivine (colored,

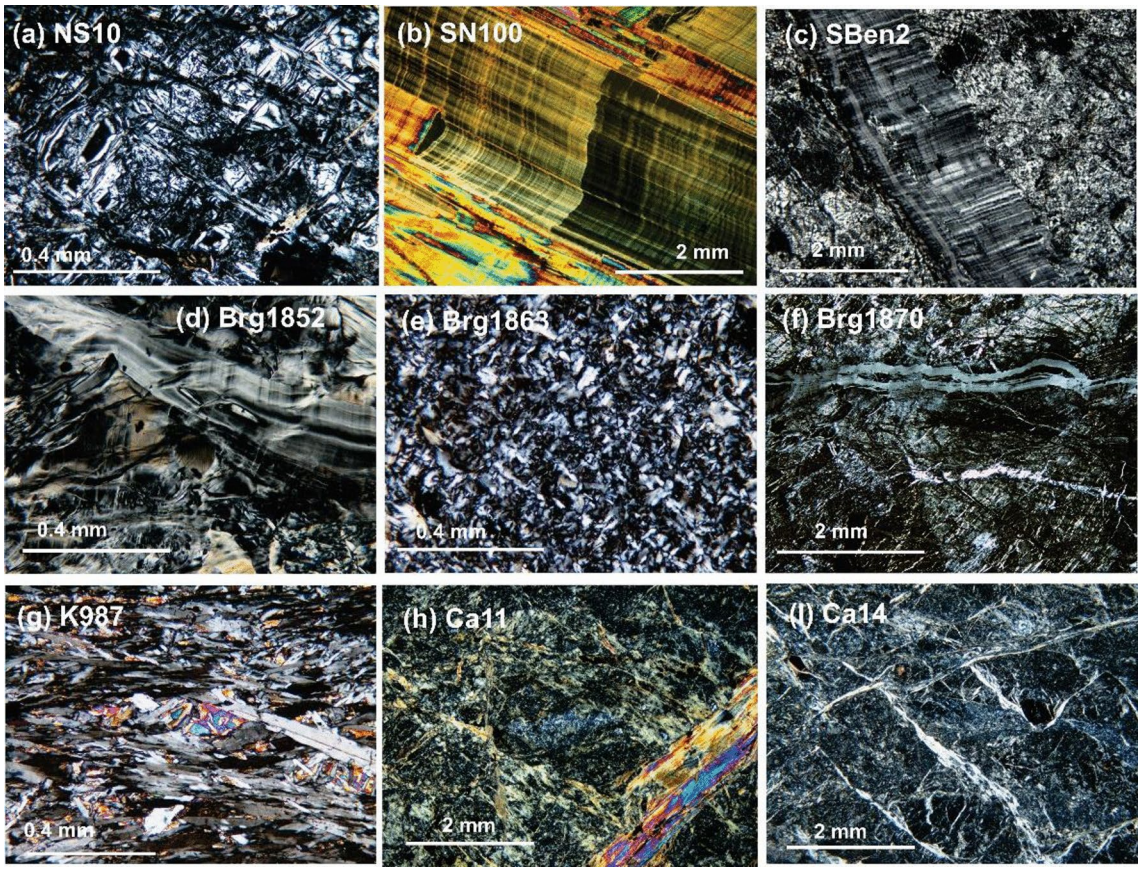

Fig. 6 Optical images of thin sections with cross-polarized light. **a** Fragmented microstructure in NS10 with different grain orientations. **b** Layer of highly aligned fibers in SN100 (slightly thicker section). **c** SBen2 with highly oriented prismatic chrysotile vein in a randomly oriented matrix of lizardite. **d** Brg1852 with oriented chrysotile on a fracture surface. **e** Randomly oriented lizardite in Brg1863 bulk matrix. **f** Heterogeneous structure in Brg1870 with 0.5–1 mm blocks of bulk lizardite and a chrysotile vein. **g** Highly oriented antigorite platelets (grey/white) in Valmalenco serpentinite K987, with olivine (high birefringence). **h** Blocky texture of antigorite in Ca11 with coarse secondary antigorite on a fracture surface. **i** Bulk matrix in Ca14 divided into blocks with serpentine and some talc on surfaces

with high order birefringence). There is not much bending of the serpentine grains, indicative of plastic deformation/recrystallization at high PT conditions. The thin section and the sample for X-ray diffraction were prepared from the same block used by Kern et al. (2015) for neutron diffraction, EBSD and velocity measurements but, as documented by (Liu et al. 2020), there are many local heterogeneities at the outcrop scale. The thin section image of Ca11 from Galicia (Fig. 6h) shows a heterogeneous matrix without clear crystal orientations but in fractures there are some highly aligned secondary crystallites. Also Ca14 (Fig. 6i) displays a largely uniform matrix but fractures in several directions in which highly oriented serpentine and some talc crystallized. Fracture spacing is on average ~ 1–2 mm. This microstructure is similar to the "crack-seal" patterns described by Viti and Mellini (1998), Andreani et al. (2004, 2005) and Viti et al. (2018).

SEM microstructures and chemical composition

Backscattered electron images (BSE) with an SEM at high contrast illustrate great complexities at the micron scale (Fig. 7). In BSE images the brightness is related mainly to composition. For California serpentinites, NS10 bulk contains magnetite (Fe_3O_4, bright) and dendritic pentlandite ($(Ni,Fe)_9S_8$, very bright) as minor phases in a matrix of serpentine (grey; Fig. 7a). Overall magnetite is concentrated in fairly randomly oriented veins (Fig. 7b). On sheared surfaces (NS11), the sample contains layers of andradite garnet ($Ca_3Fe^{3+}{}_2[SiO_4]_3$, very bright, on left) and antigorite (dark). Both layers display shape preferred orientation of grains as indicated by contrast with long axes extended in the bottom-left, top-right 45º direction (Fig. 7c). Sample MW1 contains a mixture of chlorite (brighter grey) and antigorite (darker), with equiaxed magnetite (bright) (Fig. 7d). There is no distinct orientation pattern of the two phases, at least not on the scale of the image.

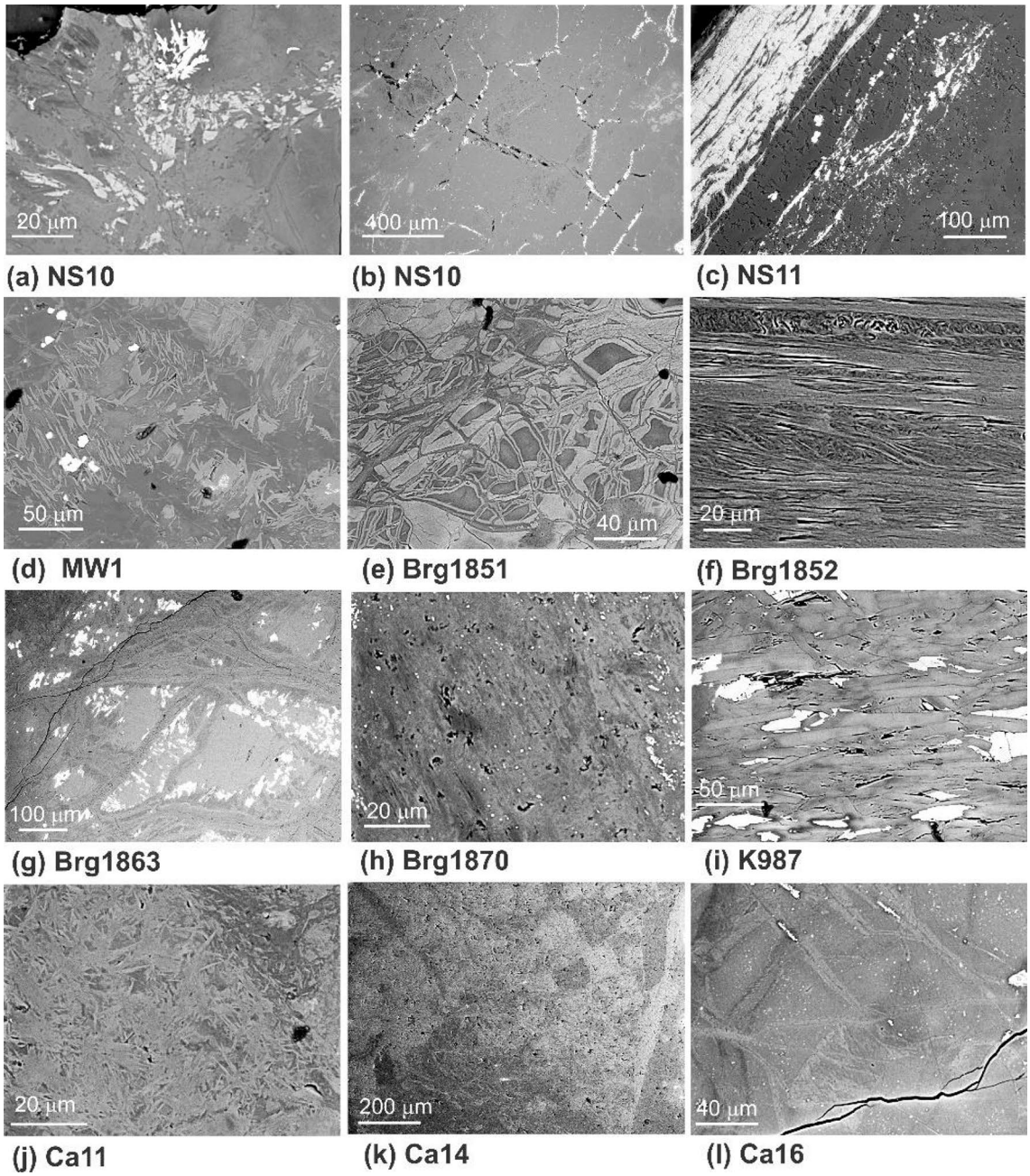

Fig. 7 Some high-contrast SEM-BES images of microstructures. **a** Microstructure with dendritic pentlandite (bright) and magnetite (bright grey). **b** Homogeneous bulk microstructure with magnetite on fractures. **c** Surface structure with bright andradite and aligned dark serpentine. Bright dots are magnetite. **d** Elongated chlorite (brighter) and serpentine (darker). Bright dots are magnetite. **e** Bulk with zoned serpentine fragments. **f** Surface structure with highly aligned crystals and layer with tubular serpentine that are aggregates of nanometer-scale chrysotile. **g** Complex serpentine microstructure with interstitial calcite (bright) in blocks of serpentine and chlorite. **h** Fairly aligned serpentine in the bulk of this sample. **i** Well-aligned antigorite platelets with flattened olivine (bright). **j** Randomly oriented serpentine crystals. **k** Blocky texture with slight variations in brightness due to some compositional zoning. **l** Homogeneous bulk structure with fairly large serpentine crystals

In the Alps, lizardite in sample Brg1851 shows a blocky mesh texture perhaps transforming from original olivine grains (Viti and Mellini 1998). In the BSE image at very high contrast the center is darker, and the rim is brighter (Fig. 7e). Such contrast in BSE image brightness is associated with slight differences in Al and Fe concentrations in the serpentine minerals as shown in the EDS maps in Fig. 8. In Fig. 8 the central parts of the blocky serpentines have a fairly pure Mg–Si composition, and the rim is enriched in Al and Fe, depleting both Mg and Si. Table 3

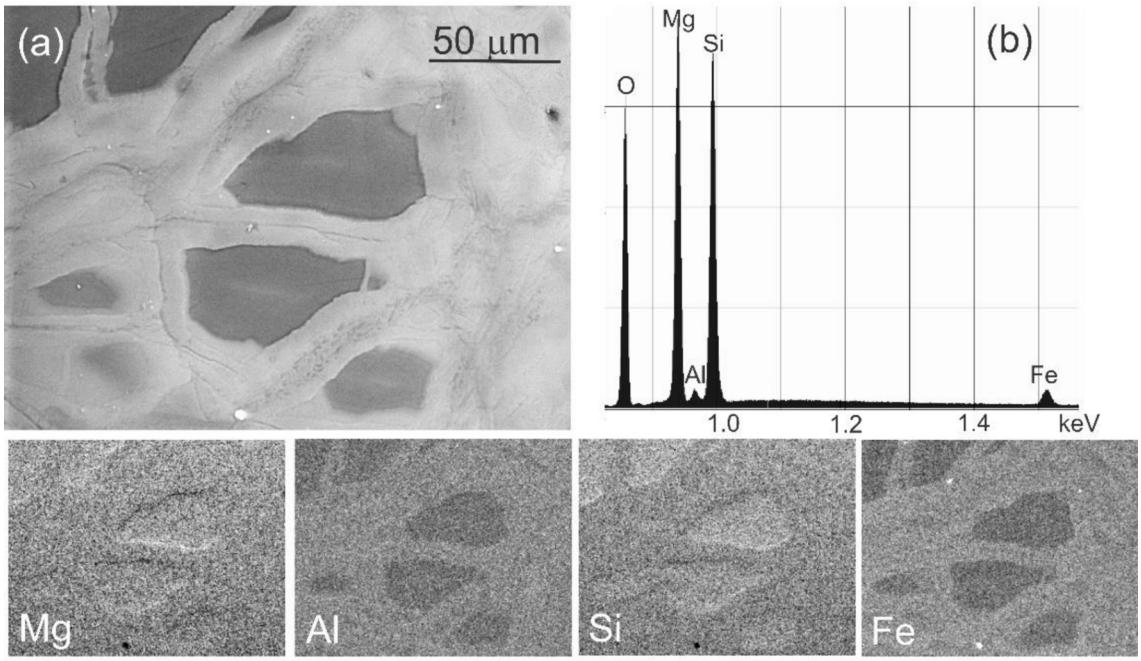

Fig. 8 **a** Very high contrast backscatter SEM-BE image of serpentinite Brg1851 displaying strong variations in brightness (compare with **e**). **b** EDS spectrum of spot analysis on bright area, mainly O, Mg, and Si but some Al and Fe. (bottom) EDS scans with long integration time for Mg, Al, Si and Fe. These elemental concentration maps show that the differences in BE image brightness are linked to elemental abundance differences in Al and Fe

gives approximate formulas. This shows that the tetrahedral sites are not pure Si, some having been replaced by Al. In Brg1851, this occurs more towards the rim, as the maps indicate.

Sample Brg1852, which is from a sheared surface of bulk Brg1851, shows a complex texture in the BSE image with overall well-aligned serpentine zones, each containing finer fibrous components which are about 2 µm in diameter (top of Fig. 7f). TEM images identify them as chrysotile and polyhedral serpentine (cf. Fig. 9 c,d). By contrast, sample Brg1863 is fairly heterogeneous with deformed serpentine blocks (darker and brighter grey) and interstitial dolomite (bright) (Fig. 7g). Brg1870 displays a more oriented microstructure of serpentine (Fig. 7h). Individual crystals are about 10 µm long and 1 µm thick. For sample K987 the SEM image shows a similar texture to that observed with the optical microscope (Fig. 6e) where antigorite (grey) and olivine (brighter) are well foliated (Fig. 7i). Individual antigorite grains are about 50 µm long and 5 µm thick, olivine grains are ~ 30 × 10 µm. Both are strongly aligned. In samples as these, EBSD for texture analysis is applicable.

Sample Ca11 from Northern Spain has randomly oriented serpentine platelets (~ 1 × 10 µm) (Fig. 7j). The image of Ca14 displays serpentine of different brightness that can be attributed to slightly different Fe-content (see below), particularly in a secondary vein on the right side (Fig. 7k). The image of Ca16 (Fig. 7l) shows a homogeneous region with randomly oriented serpentine platelets with sizes slightly larger those in Ca11 (4–40 µm). Be aware that all these microstructures are on the ~ 100 µm scale, considerably smaller than the 10 mm scale of the samples analyzed for texture with synchrotron X-rays, which averages these fine-scale structures over large volumes.

Energy-dispersive X-ray spectroscopy (EDS) with an SEM was used to analyze compositions and identify serpentine, chlorite, and other accessory phases (andradite, diopside, olivine, magnetite, pentlandite) listed in Table 2. In Table 3 we normalized cation percentages of Mg, Fe, Si and Al for serpentine to 5.0, corresponding to the idealized formula $(Mg, Fe)_3(Si, Al)_2O_5(OH)_4$ (Table 3). Note that some Si + Al values exceed 2.0. This is due to the resolution of the EDS analyses. The Al content of serpentine ranges from 0–1.7%, Fe from 0.6–1.8%. Spot analyses were performed on brighter and darker regions of BE-SEM images. Brighter regions have generally a higher iron content, but brightness also depends on crystal orientation. Al-substitution in serpentine may be significant for the P–T stability (e.g. Bromiley and Pawley 2003; Padrón-Navarta et al. 2013; Page 1968).

As mentioned above, this was quantified for Brg1851 by scanning over a small sector to explore chemical causes for brightness changes where the center of grains are significantly darker than edges (Fig. 8a, see also Fig. 7e). Figure 8b displays an EDS spectrum of the bright region

and the bottom are elemental scans for Mg, Al, Si and Fe. The dark regions in the BE image (Fig. 8a) correspond to Mg and Si-rich compositions, depleted in Al and Fe. The surrounding bright regions are richer in Al and Fe, and Si is slightly depleted, being replaced by Al. The differences are not large but significant: dark Si 15.17%, Al 0.44%, Fe 0.62% and bright Si 14.79%, Al 0.61%, Fe 0.89% (Table S1). Thus, the original serpentine was more pure and then partially altered by aqueous Fe and Al-containing solutions along grain boundaries. A last stage, along fractures, is again depleted in Fe (darker grey in BE-image).

Chlorite was differentiated from serpentine based on lower silicon and higher aluminum content (chlorite Al 4–6%, Si 10–12%; serpentine Al 0–1.7%, Si 13–15%). Most chlorites have clinochlore composition (low Fe). In three samples Cr was recorded (MW1, Brg758 and Brg1863).

TEM microstructures

Yada (1971) was one of the seminal papers documenting the tubular structure of chrysotile (Fig. 1c) that inspired high resolution transmission electron microscopy of serpentine, illustrating complex structures of coexisting polytypes and a wide range of polysomes, as well as stacking faults and intergrowths with other sheet silicates (e.g., in chronological order, Langer et al. 1974; Yada 1979; Veblen and Buseck 1979; Mellini et al. 1987; Otten 1993; Banfield et al. 1994, 1995; Banfield and Bailey 1996; Dodoni et al. 2002; Dodoni and Buseck 2004; Auzende et al. 2002, 2006b; Gualtieri et al. 2012; Zhang et al. 2021).

Here we explore microstructures of a few of our samples with the TEM. With a much higher spatial resolution than optical microscopy and SEM, the transmission electron microscopy data provide the least ambiguous identification of serpentine polymorphs and of local heterogeneities. For sample Brg1852 a slice was cut with focused ion beam (FIB) in a SEM perpendicular to striations (Fig. 7f). As a result, we were able to view the serpentine sample in a TEM along the direction of serpentine fibers. Figure 9c, d are high-resolution STEM images that show well-aligned serpentine tubes that are nearly close-packed. The curved lattice structure about the tube axes is diagnostic of chrysotile/polyhedral serpentine (Fig. 1c). The white areas in the center indicate hollow regions in the center of the tubes. Similar tubular structures were also identified in samples SN100 (Fig. 9a) and SBen2 (Fig. 9b), though there is no strong parallel alignment, and some scrolls are perpendicular to the view. In samples Ca14 and Her1, antigorite is the dominant polymorph, as evidenced by the wavy texture in the TEM images as a result of periodic switching of tetrahedral layers between the two sides of the octahedral layers (Fig. 9e, f and Fig. 1d; e.g. Capitani and Mellini 2004). These high resolution images also display an abundance of stacking faults and misorientations, indicating that serpentine is far from a perfect single crystal.

The detailed TEM images provide evidence of deformation and crystal orientation heterogeneity. Crystals in Brg1852 transform from chrysotile to polyhedral serpentine. In samples SN100 and SBen2, the orientations of the tubular crystals vary significantly and there could be intergrowths of lizardite and chrysotile. Samples SN100, Brg1852 and Her1 appear fibrous in hand specimens (Fig. 2c, h, o) but they develop complex twinning and stacking faults at nanoscale.

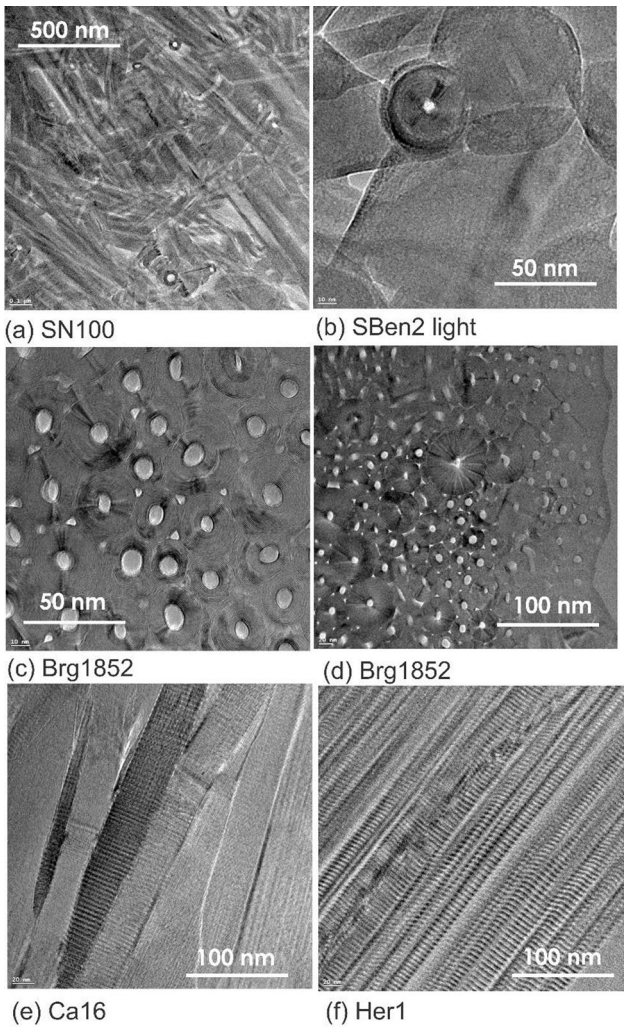

Fig. 9 High resolution TEM images of microstructures in some serpentine samples. **a** SN100 with chrysotile but complex alignment. Some tubes are vertical. **b** SBen2 vein. Chrysotile/polyhedral tube surrounded by prismatic crystals. **c**, **d** Brg1852. Parallel tubular structures of chrysotile and polyhedral serpentine viewed along the tube axis. The centers of the tubes are hollow. **e** Ca16. This aggregate of prismatic crystals is composed of antigorite with stacking faults and dislocations. **f** Her1 with complex microstructures of antigorite, with many defects and misorientations

Preferred orientation

While optical and electron microscopy qualitatively illustrate the mineral assemblage, serpentine polymorphism, and microstructure of the serpentinite samples, the synchrotron X-ray bulk diffraction data allow quantitative determination of the crystallographic preferred orientation averaged over significant sample volumes (~10–25 mm^3). Because the analyses are based on least squares refinements on measured diffraction images, the method requires that we have prior knowledge on the existing mineral phases in the bulk samples. For the serpentinites investigated in this study, we relied mainly on SEM analyses to identify secondary mineral phases such as chlorite, magnetite, pentlandite, dolomite and andradite.

Figures 10, 11, 12 show pole figures obtained from 3D orientation distributions with the Rietveld refinement. As mentioned earlier, orientation distributions were manually rotated to make them easier to compare. For Figs. 10 and 11 they were rotated such that the sheet-plane maximum (001) is in the center of the pole figure and the chain direction maximum (010) for monoclinic and (110) for trigonal in the E-W direction. For the fibrous samples in Fig. 12 the fiber direction is in the center, [100] for chrysotile and [010] for antigorite.

We only show two pole figures (001) and (010) for monoclinic antigorite and chlorite (second setting, corresponding to 100 and 001 first setting), (0001) and (11–20) for trigonal lizardite and {001} and {110} for cubic andradite (NS11).

For serpentine the (001) and (0001) directions correspond to poles to serpentine sheet planes, whereas the [010] (close to (010) poles) and [11–20] directions correspond to serpentine tetrahedral chain directions (Fig. 1a, vertical). The same pole density scale (2.5–0.4 multiples of random distribution, mrd) was applied to all in Figs. 10 and 11 to make comparisons straightforward. The only exception is the scale for sample K987 which has a much stronger texture (16–0.15 mrd, log-scale was used). Pole density maxima and minima for (001) and (0001), as well as ODF maximum and Texture index J (Bunge 1982, p. 88) are listed in Table 4. The (001) maxima are also indicated in Figs. 10 and 11.

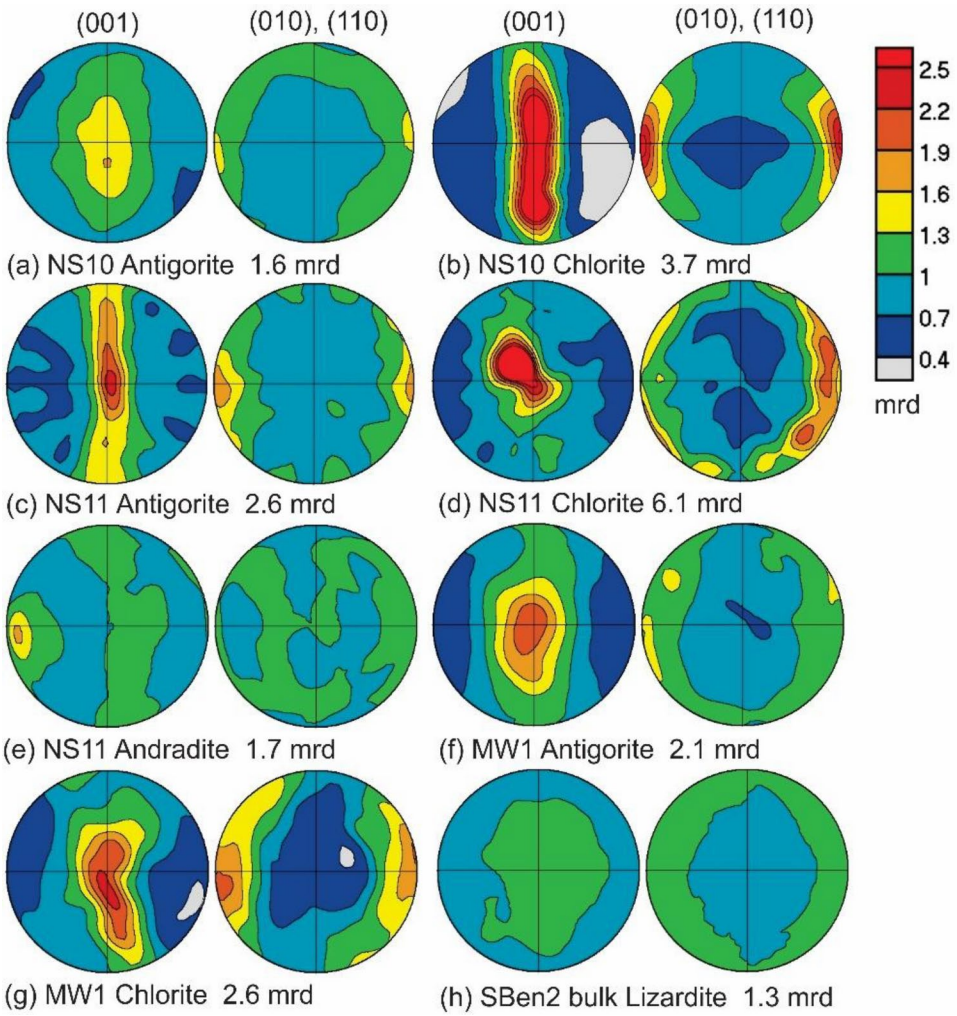

Fig. 10 Pole figures (001) and (010) for antigorite and chlorite, and (001 and (110) for lizardite from California serpentinites, projected on the approximate foliation plane. Same linear pole density scale for all samples. Andradite is cubic and (001) and (110) pole figures are shown. Equal area projection. Maximum pole density in multiples of random distribution (mrd) is indicated for each sample

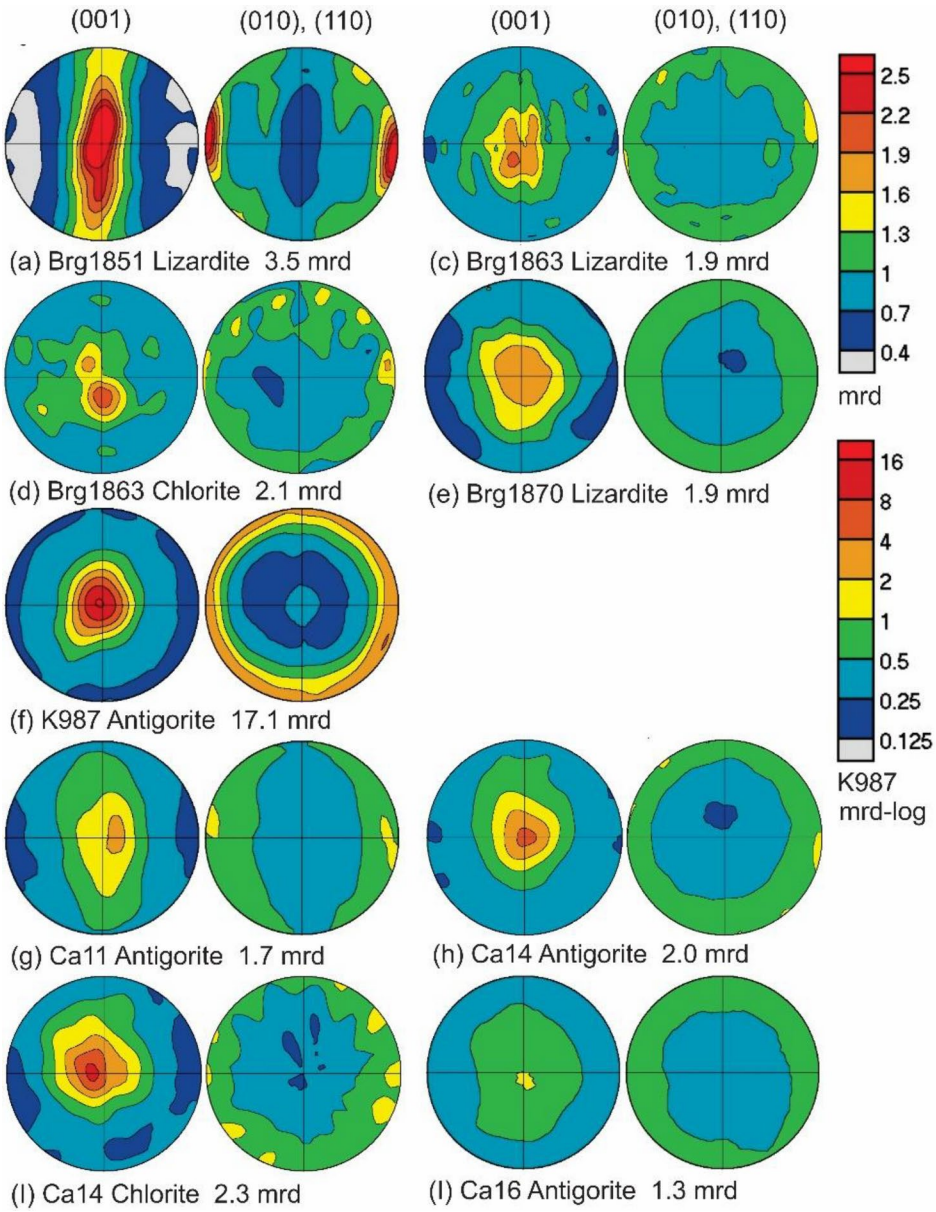

Fig. 11 Pole figures (001) and (010) for antigorite, chlorite, and (001) and (110) for lizardite from the Alps and Northern Spain, projected on the approximate foliation plane. Same linear pole density scale for all samples except K978 with logarithmic scale. Equal area projection. Maximum pole density in multiples of random distribution (mrd) is indicated for each sample

(001) pole density maxima for bulk serpentinite range from 1.3 (SBen2 bulk) to 3.5 mrd (Brg1851), except for K987 antigorite with a maximum of 17.1 mrd. For chlorite maxima range from 2.1 (Brg1863) to 3.7 mrd (NS10b). In samples with chlorite, chlorite has a stronger crystal alignment than serpentine, presumably due to a more homogeneous microstructure. Examples are NS10, NS11, MW1, Brg1863 and Ca14. On surfaces and in veins crystals are more strongly aligned, e.g. in NS10 bulk antigorite 1.6 mrd compared with NS11 surface 2.6 mrd, and NS10 bulk chlorite 3.7 mrd and NS11 surface 6.1 mrd (Fig. 10). Distributions with maxima less than 2 mrd can be considered to be close to a random distribution (1.0 mrd). In sample NS11 the surface is mainly composed of cubic andradite which has a very weak preferred orientation (1.7 mrd).

Most bulk samples have a fairly circular pole density distribution in (001) pole figures, but in some there is an ellipsoidal distortion (e.g. NS10, MW1 and Brg1851). Similar distributions are observed for other sheet silicates, e.g. in slates and schists with sheet planes tilting around the lineation direction due to a 3-dimensional deformation history (e.g. Wenk et al. 2010, 2022). It is extreme in sample Brg1851 which was measured close to a fracture surface with a strong shear component. Penetrative homogeneous deformation with a clear foliation is achieved locally such as in small serpentinite slabs entrenched in Franciscan mélange like MW1, tectonic plastic deformation in the Platta nappe like Brg1870, or recrystallization under stress at high temperature as in Valmalenco antigorite K987.

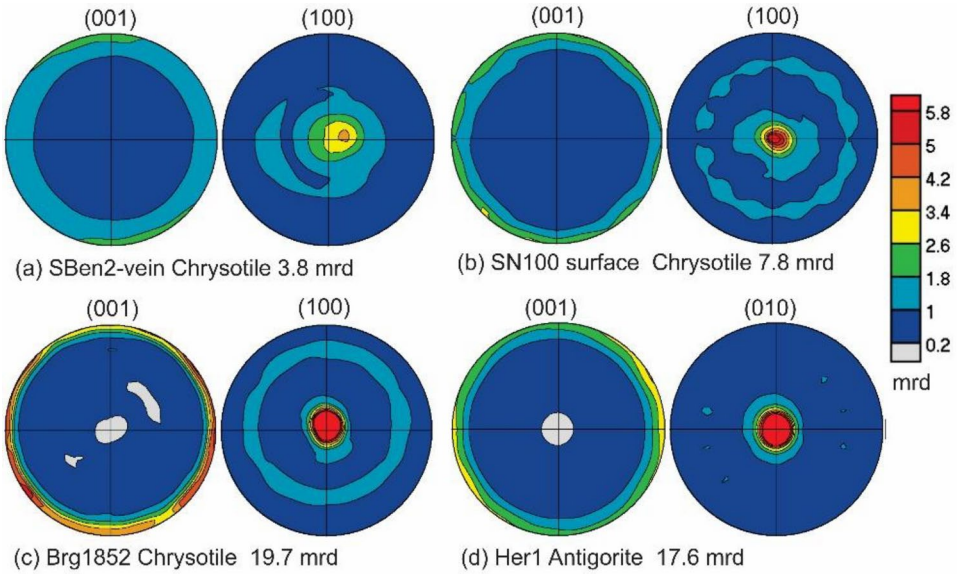

Fig. 12 Pole figures of fibrous serpentine projected along the fiber axis. Same linear pole density scale for all samples. Equal area projection. Maximum pole density in multiples of random distribution (mrd) is indicated for each sample

Table 4 Sample volume fractions from MAUD used for velocity averaging

Sample	Volume fraction %	001 max (mrd)	001 min (mrd)	ODF max (mrd)	J
California					
NS10-bulk	Ant 68%	1.6	0.6	2.4	1.06
NS10-bulk	Chl 32%	3.5	0.3	4.8	1.70
NS11-surface	Ant 17%	2.4	0.6	4.1	1.17
NS11-surface	Chl 7%	5.5	0.4	9.3	1.51
NS11 surface	And 76%	1.7	0.8	2.3	1.04
MW1	Ant 57%	2.2	0.4	2.7	1.19
MW1	Chl 43%	2.4	0.4	4.6	1.34
SBen2 bulk	Liz	1.3	0.8	1.2	1.01
SBen2 vein	Liz	1.9	0.4	2.4	1.16
Central Alps					
Brg758	Ant	15.0	0	163.6	14.60
Brg758	Liz	13.8	0	33.7	5.27
Brg758	Chrys	17.0	0	174.0	18.16
Brg1851 bulk	Liz	3.5	0.3	16.3	1.61
Brg1852surface	Chrys	8.9	0.1	12.8	2.90
Brg1863	Liz 69%	2.1	0.5	4.1	1.07
Brg1863	Chl 31%	2.1	0.6	5.2	1.17
Brg1870	Liz	1.9	0.6	2.3	1.13
K987	Ant	17.1	0.1	21.5	6.42
Spain					
Ca11	Ant	1.7	0.6	1.9	1.07
Ca14	Ant 70%	2.0	0.7	2.5	1.09
Ca14	Chl 30%	2.3	0.6	2.5	1.20
Ca16	Ant	1.3	0.8	1.6	1.02
Her1	Ant	17.6	0.1	25.1	2.89

Texture information (001) max and min in mrd, ODF max and OD Texture Index J (Bunge 1982). Ant: antigorite, Liz: lizardite, Chrys: chrysotile, Chl: chlorite, And: andradite

Figure 12 compares pole figures of 4 samples with fibrous morphology (Fig. 2c, e, h, o). Based on TEM results (Fig. 9) SBen2 from a secondary vein, SN100 and Brg1852 display tubular morphologies defining them as chrysotile. They all have a (100) maximum in the center of the pole figures which is close to the [100] fiber axis (e.g. Jagodzinski and Kunze 1954; Whittaker 1956), whereas Her1 is antigorite with elongated crystallites, with a (010) maximum and a [010] fiber direction (e.g. Kunze 1956). While all other samples show a maximum of (001) sheet plane normals, these fibrous samples display a strong maximum of the fiber directions [100] and [010]. It is an example where the pole figures can be used to define the crystallite microstructure and polymorphism.

Elastic anisotropy

From orientation distributions of component minerals corresponding linear elastic properties can be calculated by averaging over single crystal elastic properties. Linear elastic properties are described with the twice-symmetric fourth-rank stiffness tensor C_{ijkl} (or compliance S_{ijkl}, which satisfies the "inversion relation" $C_{ijkl} \equiv S_{ijkl}^{-1}$). In the general case the tensor has 21 independent components (e.g. Nye 1985).

The averaging can be done as an arithmetic average of stiffness over all crystals (Voigt average, Voigt 1887) or an average of compliance (Reuss average, Reuss 1929). A Voigt average is higher (upper bound of the polycrystal properties) than the Reuss average (lower bound). The real elastic properties of the polycrystal are between the two. Here we use the geometric mean model (Matthies and Humbert 1995) that obeys the statistically important group principle (Matthies et al. 2001).

Another approach is to use an iterative self-consistent algorithm that calculates elastic properties of the polycrystal, treating it as an effective medium composed of grains approximated by ellipsoidal inclusions (e.g. Kröner 1958). This has been applied to slates with highly anisotropic grain shapes (Wenk et al. 2022) and can be done with the self-consistent method GeoMIXself (GMS) (Matthies 2010, 2012). But the slate study documented that grain shapes have only a small effect on anisotropy and are thus irrelevant for serpentinites.

Volume fractions of minerals are available from the Rietveld refinement (Table 4), and single crystal elastic constants of minerals are taken from the literature (Suppl. Table 2). We are using first principles results for antigorite (Satta et al. 2022; see also Bezacier et al. 2010, 2013), lizardite (Deng et al. 2022; see also Auzende et al. 2006a; Mookherjee and Stixrude 2009) and chlorite (Mookherjee and Mainprice 2014; see also Ulian et al. 2018) based on ideal crystal structures using the generalized gradient approximation (GGA, Perdew et al. 1996). These models also investigate changes with pressure (Supplementary Table 2). For our calculations we assume ambient conditions.

From elastic properties, anisotropic seismic wave velocities can be calculated in different directions and represented as pole figures. Supplementary Fig. 2a displays P-wave distributions for single crystals in spherical projections at ambient conditions. Lizardite is most anisotropic, chlorite is least anisotropic. P-waves propagating perpendicular to the sheet plane are slowest. The high anisotropy of lizardite is based on a simple ideal structure. All minerals considered here are not ideal but contain stacking faults, polysomatism and dislocations which will reduce anisotropy (e.g. Fig. 9). Also, first principles studies document that anisotropy is considerably reduced with increasing pressure. Particularly the weak stiffness perpendicular to the sheet plane greatly increases with pressure. Thus, our values for bulk anisotropy provide an upper limit that is likely reduced, particularly in the deeper Earth.

Using mineral stiffnesses, densities, orientation distributions and phase fractions elastic properties have been calculated as a geometric mean (Table 5) and from it wave velocities have been derived with BEARTEX (Wenk et al. 1998) as described in Sect. 4.3. Elastic anisotropy (An) can be qualitatively described using P-wave velocities as $An\% = 200(V_{Pmax} - V_{Pmin})/(V_{Pmax} + V_{Pmin})$.

Distributions of P-wave velocities for bulk samples are shown in Fig. 13a–j in the same orientation as crystal orientation pole figures (Figs. 10 and 11). In all serpentinites,

Table 5 Elastic properties of bulk serpentinites obtained by geometric mean averaging, expressed as 21 stiffness coefficients (C_{ij} in GPa); wave velocity maxima and minima (P and dS velocities) are in km/s; P-wave anisotropy coefficient An (%); density (g/cm^3)

	NS10	MW1	SBen2	Brg1851	Brg1863	Brg1870	K987	Ca11	Ca14	Ca16
Density	2.55	2.55	2.5	2.55	2.5	2.5	2.55	2.5	2.5	2.5
C_{11}	136.5	141.6	104.6	135.7	118.8	112.6	159.1	127.3	119.1	121.6
C_{22}	126.3	128.7	102.5	99.1	117.2	107.4	154.2	119.0	115.8	120.3
C_{33}	119.4	120.0	98.8	85.9	107.2	89.2	89.6	111.8	102.3	115.1
C_{44}	38.0	37.8	30.0	26.1	33.0	28.2	25.4	35.2	30.2	36.2
C_{55}	38.2	39.3	30.2	28.2	33.3	29.1	24.9	36.3	31.0	36.3
C_{66}	40.8	42.9	31.1	33.5	35.9	33.4	52.9	38.5	35.3	37.6
C_{12}	47.1	48.8	41.3	42.0	44.7	42.5	51.5	45.6	46.9	45.4
C_{13}	46.2	47.2	40.8	38.3	43.5	40.1	34.9	44.7	45.7	44.9
C_{14}	0.2	0.3	−0.1	0.1	−0.04	0.3	−0.7	0.1	−0.1	0.1
C_{15}	−0.1	0.2	−0.5	0.6	0.2	−0.2	2.5	−0.7	0.9	−0.2
C_{16}	−0.04	−0.1	−0.3	−1.2	0.1	0.5	−0.9	0.3	0.1	0.04
C_{23}	47.7	47.6	40.7	38.5	43.4	39.6	35.8	44.6	45.5	45.0
C_{24}	0.2	0.3	−0.3	0.1	−0.03	0.1	−1.1	−0.1	−1.2	0.2
C_{25}	0.1	0.2	−0.1	0.02	0.1	−0.2	0.3	−0.1	−0.1	−0.1
C_{26}	−0.4	−0.5	−0.3	−0.2	0.2	−0.1	−0.7	0.2	0.2	0.1
C_{34}	0.3	0.5	−0.4	0.5	−0.5	0.03	0.0	0.03	−1.1	0.03
C_{35}	0.2	−0.02	−0.5	0.05	0.1	−0.4	0.02	−0.3	0.4	0.1
C_{36}	−0.1	−0.1	−0.03	0.1	−0.01	−0.1	0.3	0.03	−0.1	0.02
C_{45}	−0.2	−0.1	−0.1	0.01	0.02	−0.04	0.01	0.1	0.01	−0.01
C_{46}	0.1	0.4	−0.2	0.07	0.1	−0.3	0.7	−0.2	0.2	−0.1
C_{56}	0.3	0.6	−0.2	0.2	−0.1	0.3	−0.7	0.1	−0.7	0.1
VPmax	7.99	7.45	6.41	7.29	6.82	6.64	7.84	7.00	6.83	6.83
VPmin	7.27	6.85	6.21	5.80	6.47	5.91	5.85	6.55	6.31	6.65
An(%)	9.5	8.4	3.2	22.8	5.3	11.6	29.1	6.6	7.9	2.7
dS max	0.34	0.26	0.07	0.55	0.19	0.31	1.42	0.17	0.28	0.08

Values assume ambient conditions

slowest P-waves are perpendicular to the "foliation plane", corresponding to the preferred orientation of (001) normals of sheet silicates. Notice that in most there is no axial symmetry in the P-wave distributions. An exception is K987 with the strongest anisotropy (29%).

Figure 13k–t displays plots of shear-wave splitting (difference between fast and slow shear wave velocities). Dark lines in the shear-wave splitting plots indicate the orientation of the fast S-wave. Highest shear-wave splitting is in the XY plane. Also, here highest shear-wave splitting is observed in K987 (1.4 km/s), for all others it ranges from 0.07 to 0.55 km/s (Table 5).

Discussion

First a few comments about methods to measure CPO in serpentinites. Conventionally this was done with an optical microscope equipped with a universal stage on thin sections (e.g. Soda and Takagi 2010). A fairly large crystal size is required (>0.1 mm) which is observed in recrystallized antigorite serpentinites. Most recent studies have used electron back-scatter diffraction (EBSD) which can be done on smaller grain size but also relies on well-crystallized grains and scans are done over areas ranging from 0.1 × 0.1 mm to 10 × 10 mm to obtain sufficient grain statistics. It is generally not feasible for lizardite with defects and chrysotile with bending of lattice planes.

Here we used high energy X-rays on cylindrical samples 2–3 mm in diameter and 10 mm long. This provides good grain statistics but requires rather sophisticated data

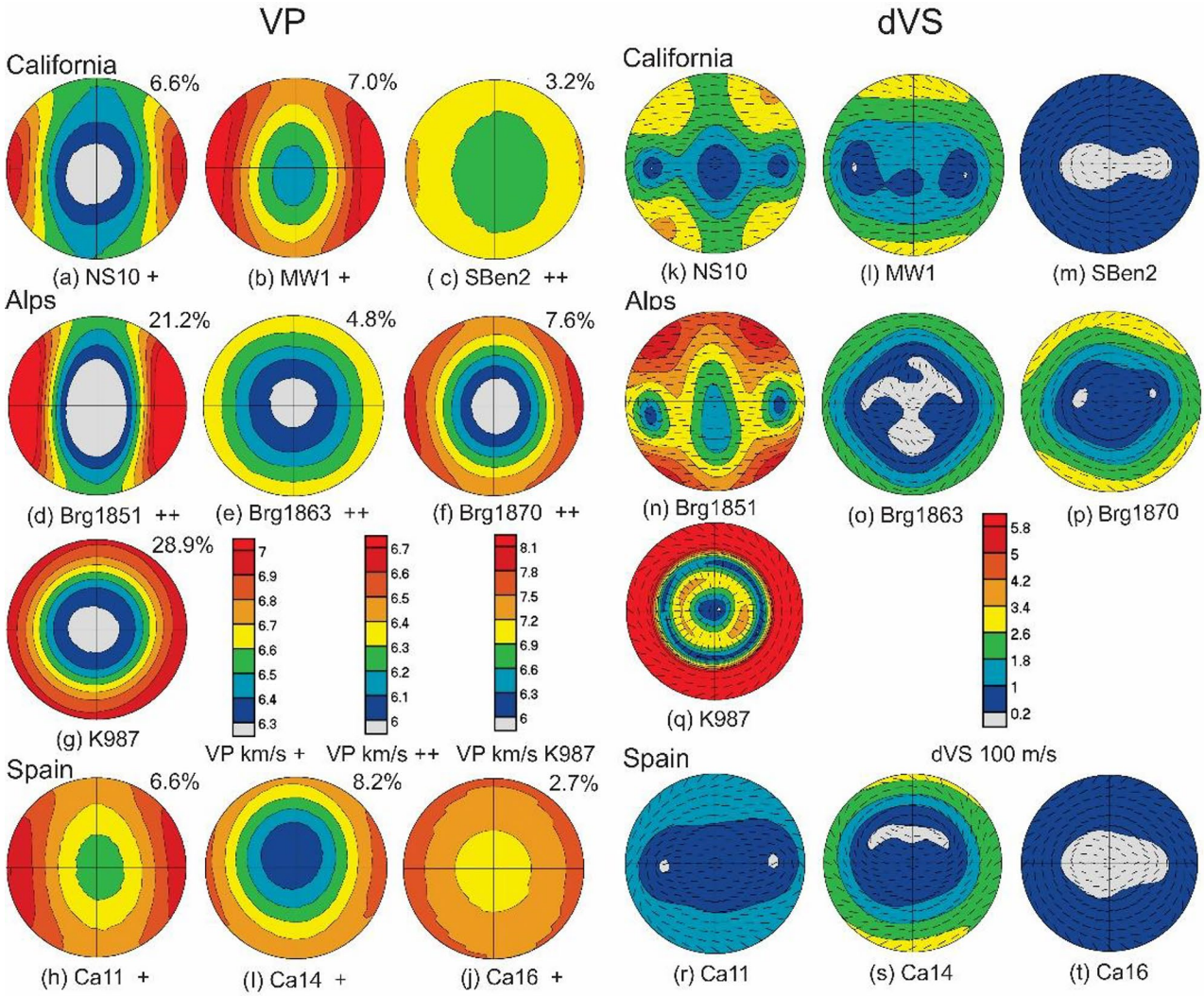

Fig. 13 **a**–**j** P-wave velocities VP for bulk serpentinites projected on foliation plane (same orientation as pole figures in Figs. 10, 11). Different scales are used for antigorite (+) and lizardite (++) and for the highly anisotropic sample K987. Also indicated is bulk anisotropy in %. **k**–**t** Shear-wave splitting (dVS). Lines in dS plots indicate orientation of the fast S-wave. Equal area projection

analysis. This method can be applied to all serpentine polymorphs. Yet another method is neutron diffraction with very high sample penetration (1–5 cm).

Methods have been compared (optical, EBSD and X-ray) for Toba serpentinites and reasonable agreement was achieved but X-rays provided better statistics (Soda and Wenk 2014). EBSD often emphasizes some large grains. Neutrons and X-rays were compared for Valmalenco serpentinite (Kern et al. 2015). Both provided similar results but the peak to background ratio was much better for X-rays than neutrons because of hydrogen scattering.

The serpentinite samples investigated in this study come from a variety of geological settings and formed in conditions that span a large range of pressure, temperature and tectonic history. The petrographic and electron microscopic observations of the samples at different scales show that serpentinites are very heterogeneous, and they often formed in different generations, as evidenced by compositional zoning, secondary veins and fractures, where younger serpentine precipitated and was deformed (e.g. Fig. 7). Such complexities are also ubiquitous on the outcrop scale (Fig. 2a, f, i, k) and in thin sections (e.g. Fig. 6b, d, e, d, j, n). Serpentinites examined in this study rarely extend over large distances. They form generally fairly narrow layers, often broken up into patches and locally stretched out with foliation development like MW1 along the San Andreas fault or NS10 along the Melones fault in California.

TEM data highlight heterogeneities at the microscopic scale with intergrowths of serpentine polymorphs, and with chlorite as was also reported in other serpentinites (e.g. Wunder et al. 2001; Zhang et al. 2021). The detection of more than one type of polymorph at the micron scale suggests that the formation was not at thermodynamic equilibrium conditions, but likely kinetically controlled (e.g. Evans 2010). In addition to polymorphism, polytypism plays a role, with antigorite showing ubiquitous variations in wave-repeat. There are many stacking faults and dislocations (Fig. 9). Particularly lizardite is clearly not a homogeneous sheet as is mica or chlorite. This will affect elastic properties which have all been based on first principles calculations assuming ideal crystal structures (Suppl. Fig. 2). In real serpentine elastic anisotropy is likely considerably weaker.

The X-ray bulk sample diffraction data show that for many samples CPO is weak (1.5–3 mrd; Figs. 10, 11), and correspondingly calculated seismic anisotropy is low (Fig. 13). For those samples that do have a stronger preferred serpentine orientation such as NS10 bulk (Fig. 10a) and MW1 (Fig. 10f), the degree of serpentine alignment in (001) pole figures is still less than 3.5 mrd. Brg1851 (Fig. 11a, 3.5 mrd) was actually measured on a fragment close to the fracture surface and thus high CPO and anisotropy do not represent the bulk material.

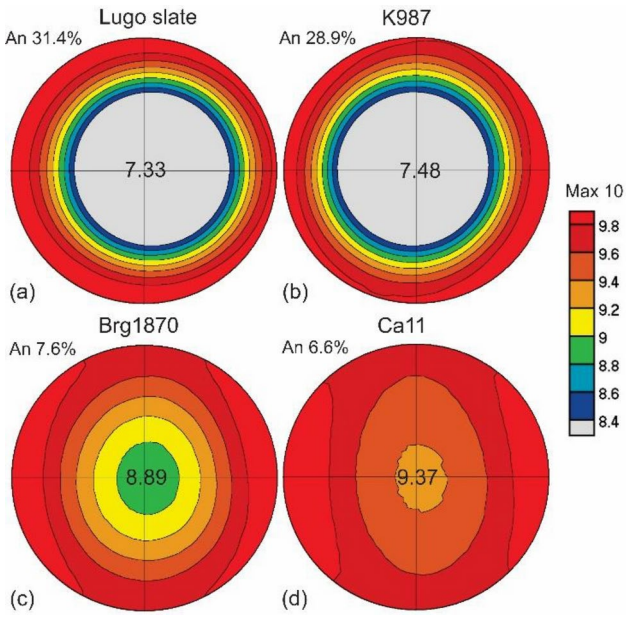

Fig. 14 Relative P-wave velocities for **a** Slate from Lugo, Spain (Wenk et al. 2022), **b** antigorite serpentinite K987 from Valmalenco, **c** lizardite serpentinite Brg1870 from the Alps and **d** Ca11 antigorite serpentinite from Spain. All distributions are normalized so that the maximum is 10. The minimum is indicated in the center. Anisotropies % are listed. Equal area projection

Sample K987 is a high-grade olivine-antigorite serpentinite from Valmalenco (Fig. 11f) yielding a (001) maximum for antigorite of 17 mrd which is similar to previous results (Kern et al. 2015), with X-rays on another sample (13.2 mrd) and neutrons on a larger sample (13.6 mrd). The resulting P-wave anisotropy of 28.9% is similar to 33% reported by Liu et al. (2020) based on EBSD measurements on small antigorite-rich patches.

Serpentinite zones can be compared with surrounding schists and slates that are highly anisotropic (e.g. Wenk et al. 2010, 2019, 2020). Figure 14 compares P wave velocities of Lugo slate from the Lower Cambrian Cándana Unit in Northern Spain (Wenk et al. 2022) with some serpentinites using normalized P-waves where the maximum is 10. The calculated P wave anisotropy for slate is 31.4% (Fig. 14a), higher than antigorite serpentinite (K987, 28.9%, Fig. 14b). Other samples which still have significant preferred orientation have much weaker anisotropies (Brg1870, 7.6% and Ca11, 6.6%, Fig. 14c, d).

Elastic properties obtained by acoustic measurements can be compared with those based on CPO data on the same samples. This has been done by performing acoustic measurements of compressional and shear wave velocities on antigorite serpentinites from Japan on cubes up to 180 MPa (Watanabe et al. 2014), on serpentinite from China (Ji et al. 2013; Shao et al. 2014) on 2.5 cm diameter cylinders up to 600 MPa and on sample K987 from Valmalenco both on

5 cm diameter cubes and 5 cm spheres at pressures up to 600 MPa (Kern et al. 2015). At ambient conditions velocities are lower and anisotropy is higher due to microfractures, but above 300 MPa porosity is largely closed. At these moderate pressures modeled elastic properties of bulk rocks, based on CPO and elastic properties of single crystals, are similar to those based on measured wave velocities.

CPO is therefore a straightforward way to assess bulk elastic anisotropy in serpentinites and was used in our study (Table 5). Obtaining reliable elastic properties of crustal and mantle lithologies is essential for better understanding the rheology of the solid Earth as well as interpreting seismic observations. Trench-parallel anisotropy was observed in Northern Spain (e.g. Acevedo et al. 2021; Barruol et al. 1998; Díaz et al. 2006; Ruiz et al. 2017) and serpentinites may indeed contribute to it as suggested by the authors, but they have relatively small volumes and very weak anisotropy (Fig. 13h–j) compared with slates (Wenk et al. 2022). The same applies to serpentinites in western North America and the Alps, where also slates and schists may contribute significantly to anisotropy. It should be mentioned again that anisotropies in Table 5 are likely too high since they rely on first principles calculations on ideal single crystals and assume ambient conditions. With increasing pressure anisotropies of antigorite (Satta et al. 2022) and lizardite (Deng et al. 2022) decrease greatly because the tetrahedral-octahedral single layer sheet structure compacts. For example for antigorite at 0 GPa pressure the stiffness C_{11} (perpendicular to the sheet plane) is 85 GPa, increasing to 170 GPa at 8 GPa pressure, while C_{22} barely changes (~210 GPa) (Satta et al. 2022), becoming almost isotropic. At 4–5 GPa, in a subducting slab, antigorite anisotropy is about half the value at ambient conditions and used in Figs. 13 and 14.

At higher pressure and temperature serpentine transforms. So far most attention has been given to dehydration of serpentine and converting it to olivine, enstatite, ringwoodite/wadsleyite and at higher pressure to bridgmanite (e.g. Hilairet et al. 2007; Padrón-Navarta et al. 2010; Raleigh and Paterson 1965) but in the future one should also consider transforming serpentine to stable hydrous high pressure phases which were already explored by Ringwood and Major (1967). Phase D $MgSi_2O_4(OH)_2$ (Liu 1986; Shieh et al. 2000; Yang et al. 1997) at ~20 GPa, and phase H $MgSiO_2(OH)$ (Nishi et al. 2014; Ohira et al. 2014; Xu et al. 2022) at ~40 GPa are elastically very anisotropic. Deformation experiments on phase D document strong texture development (Rosa et al. 2013; Wu et al 2024) and may be significant for seismic heterogeneities and anisotropy in the mantle transition zone as well as the lower mantle (e.g. Durand et al. 2024).

Conclusions

This study is a first survey of serpentinite preferred orientation and elastic anisotropy in samples from a wide range of geological settings. It documents that serpentinites from California, the Alps and Spain are heterogeneous at all scales. A few samples show high crystal alignment and correspondingly high seismic anisotropy but most display only weak orientation patterns in bulk samples, as quantified with high energy synchrotron X-ray diffraction. Exceptions are surfaces on interfaces of fractures where tectonic movements occurred, and new phases precipitated and were deformed. The volume of these fracture surfaces is minimal compared with the bulk volume. Another example of high alignment is secondary crystallization of serpentine in veins. Locally high-grade recrystallized antigorite serpentinite may contribute to observed seismic anisotropy in subducting slabs, but it may not be a major factor.

Supplementary Information The online version contains supplementary material available at https://doi.org/10.1007/s00410-025-02209-5.

Acknowledgements We acknowledged access to beamline 11-ID-C of the Advanced Photon Source at Argonne National Laboratory and supported by DOE Office of Science under Contract No. DE-AC02-06CH11357. HRW is grateful to Juan Gomez-Barreiro for taking him on a field trip to Northern Spain where serpentinites used in this study were collected. We thank John Grimsich for his assistance with conducting EDS analyses with the Zeiss EVO SEM at EPS, UC Berkeley. Luca Lutterotti provided access and help with the Rietveld texture analysis. We acknowledge access to transmission electron microscopes at the Molecular Foundry of Lawrence Berkeley National Laboratory. HRW is appreciative for support from NSF (EAR-1343908, EAR2054951, EAR-2154351) and DOE-BES (DE-FG02-05ER15637), and from The Fulbright Foundation for a fellowship in Salamanca. We acknowledge help from Michelle Devoe, Jingyi Huang, Rachel Redman and Rong Yu. We are most appreciative to the Editor Othmar Müntener and two anonymous reviewers for constructive comments that helped us improve the manuscript and correct some mistakes.

Author contributions H.-R.W. designed the study; H.-R.W. and O.B. performed synchrotron experiments; H.-R.W., A.K. and Y.Z. performed SEM experiments, E.R.K. performed TEM experiments; H.-R.W., Y.Z. and A.K. wrote the paper. All authors read and approved the final manuscript.

Data availability The data in this paper, including diffraction images, will be shared on reasonable request to the corresponding author. Note that data were collected and analyzed over several years and details of experiments as well as data analysis have changed. We provide here a link to a directory for sample Ca14 measured at APS 6/27/2022 (https://seismo.berkeley.edu/~wenk/CMP2024-Serpentine) which contains the parameter file for Rietveld diffraction data analysis with MAUD (Ca14_2022-298-ibg_ant-chl-13-40.par) as well as the MAUD package 298 for Windows 64 which was used for this sample (MAUD298.zip), and screen shots of data and fit for one detector, both Plot and Plot2D (Ca14-Plots.pdf). From the directory these files can be downloaded and used as an example. The Materials Analysis Using Diffraction (MAUD) software can be accessed from the Github page of

Lutterotti (University of Trento) https://luttero.github.io/maud/, but the most recent versions have some incompatibilities with our data. The BEARTEX software used to calculate pole figures and elastic anisotropy of the phases is available at https://seismo.berkeley.edu/~wenk/TexturePage/beartex.htm/.

Declarations

Conflict of interest The authors declare no conflict of interest.

References

Acevedo J, Fernandez-Viejo G, Llana-Funez S, Lopez-Fernandez C, Olona J (2021) Upper-crustal seismic anisotropy in the Cantabrian Mountains (North Spain) from shear-wave splitting and ambient noise interferometry analysis. Seismol Res Lett 92:421–436. https://doi.org/10.1785/0220200103

Albert R, Arenas R, Sanchez-Martinez S, Gerdes A (2012) The eclogite facies gneisses of the Cabo Ortegal Complex (NW Iberian Massif): tectonothermal evolution and exhumation model. J Iberian Geol 38(2):389–406. https://doi.org/10.5209/rev_JIGE

Amiguet E, Van De Moortèle B, Cordier P, Hilairet N, Reynard B (2014) Deformation mechanisms and rheology of serpentines in experiments and in nature. J Geophys Res Solid Earth 119:4640–4655. https://doi.org/10.1002/2013JB010791

Amthauer G, Kurtz W, Rost F (1974) Chemismus und Genese des Andradits aus dem Serpentin des Val Malenco. Schweiz Mineral Petrog Mitt 54(2–3):691–706

Andreani A, Barronet A, Boullier A-M, Gratier J-P (2004) A microstructural study of a crack-seal type serpentine vein, using SEM and TEM techniques. Eur J Mineral 16:585–595

Andreani M, Boullier AM, Gratier JP (2005) Development of schistosity by dissolution–crystallization in a Californian serpentinite gouge. J Struct Geol 27:2256–2267. https://doi.org/10.1016/j.jsg.2005.08.004

Andreani M, Mevel C, Boullier A-M, Escartin J (2007) Dynamic control on serpentine crystallization in veins: constraints on hydration processes in oceanic peridotites. Geochem Geophys Geosyst. https://doi.org/10.1029/2006GC001373

Andreani M, Grauby O, Baronnet A, Muñoz M (2008) Occurrence, composition and growth of polyhedral serpentine. Eur J Miner 20:159–171. https://doi.org/10.1127/0935-1221/2008/0020-1801

Andreani M, Munoz M, Marcaillou C, Delacour A (2013) µXANES study of iron redox state in serpentine during oceanic serpentinization. Lithos 178:70–83. https://doi.org/10.1016/j.lithos.2013.04.008

Angiboust S, Agard P, Jolivet L, Beyssac O (2009) The Zermatt-Sass ophiolite: the largest (60-km wide) and deepest (c. 70–80 km) continuous slice of oceanic lithosphere detached from a subduction zone? Terra Nova 21:171–180. https://doi.org/10.1111/j.1365-3121.2009.00870.x

Auzende A-L, Devouard B, Guillot S, Daniel I, Baronnet A, Lardeaux JM (2002) Serpentinites from Central Cuba: petrology and HRTEM study. Eur J Mineral 14(5):905–914. https://doi.org/10.1127/0935-1221/2002/0014-0905

Auzende A-L, Pellenq J-M, Devouard B, Baronnet A, Grauby O (2006a) Atomistic calculations of structural and elastic properties of serpentine minerals: the case of lizardite. Phys Chem Mineral 33:266–275. https://doi.org/10.1007/s00269-006-0078-x

Auzende A-L, Guillot S, Devouard B, Baronnet A (2006b) Serpentinites in an Alpine convergent setting: effects of metamorphic grade and deformation on microstructures. Eur J Mineral 18:21–33. https://doi.org/10.1127/0935-1221/2006/0018-0021

Banfield JF, Bailey SW (1996) Formation of regularly interstratified serpentine-chlorite minerals by tetrahedral inversion in long-period serpentine polytypes. Am Mineral 81:79–91. https://doi.org/10.2138/am-1996-1-211

Banfield JF, Bailey SW, Barker WW (1994) Polysomatism, polytypism, defect microstructures, and reaction mechanisms in regularly and randomly interstratified serpentine and chlorite. Cont Mineral Petrol 117:137–150. https://doi.org/10.1007/BF00286838

Banfield JF, Bailey SW, Barker WW, Smith RC (1995) Complex polytypism; relationships between serpentine structural characteristics and deformation. Am Mineral 80:1116–1131. https://doi.org/10.2138/am-1995-11-1203

Barnes JD, Eldam R, Lee CTA, Errico JC, Loewy S, Cisneros M (2013) Petrogenesis of serpentinites from Franciscan complex, western California, USA. Lithos 178:143–157. https://doi.org/10.1016/j.lithos.2012.12.018

Barnes JD, Beltrando M, Lee CA, Cisneros M, Loewy S, Chin E (2014) Geochemistry of Alpine serpentinites from rifting to subduction: a view across paleogeographic domains and metamorphic grade. Chem Geol 389:29–47. https://doi.org/10.1016/j.chemgeo.2014.09.012

Baronnet A, Devouard B (1996) Topology and crystal growth of natural chrysotile and polygonal serpentine. J Cryst Growth 166:952–960. https://doi.org/10.1016/0022-0248(96)00042-5

Barruol G, Souriau A, Vauchez A, Díaz J, Gallart J, Tubia J, Cuevas J (1998) Lithospheric anisotropy beneath the Pyrenees from shear-wave splitting. J Geophys Res 103:30039–30053. https://doi.org/10.1029/98JB02790

Bernoulli D, Weissert H (2021) Oxygen isotopes in ophiocalcites: an ever-lasting controversy? Int J Earth Sci 110:1–8. https://doi.org/10.1007/s00531-020-01934-5

Bezacier L, Reynard B, Bass JD, Sanches-Valle C, Van den Moortèle B (2010) Elasticity of antigorite, seismic detection of serpentinites, and anisotropy in subduction zones. Earth Planet Sci Let 289:198–208. https://doi.org/10.1016/j.epsl.2009.11.009

Bezacier L, Reynard B, Cardon H, Montagnac G, Bass JD (2013) High-pressure elasticity of serpentine and seismic properties of the hydrated mantle wedge. J Geophys Res 118:1–9. https://doi.org/10.1002/jgrb.50076

Boschi C, Bonatti E, Ligi M, Brunelli D, Cipriani A, Dallai L, D'Orazio M, Früh-Green GL, Tonarini S, Barnes JD, Bedini RM (2013) Serpentinization of mantle peridotites along an uplifted lithospheric section, Mid Atlantic Ridge at 11° N. Lithos 178:3–23. https://doi.org/10.1016/j.lithos.2013.06.003

Bouilhol P, Debret B, Inglis EC, Warembourg M, Grocolas T, Rigaussier T, Villeneuve J, Burton KW (2022) Decoupling of inorganic and organic carbon during slab mantle devolatisation. Nat Commun 13:308. https://doi.org/10.1038/s41467-022-27970-0

Brigatti MF, Galán E, Theng BKG (2013) Structure and mineralogy of clay minerals. In: Developments in clay science chap 2, vol 5A. Elsevier, pp 21–80

Bromiley GD, Pawley AR (2003) The stability of antigorite in the systems MgO–SiO_2–H_2O (MSH) and MgO–Al_2O_3–SiO_2–H_2O (MASH): the effects of Al^{3+} substitution on high-pressure stability. Am Mineral 88:99–108. https://doi.org/10.2138/am-2003-0113

Brownlee SJ, Hacker BR, Harlow GE, Seward G (2013) Seismic signatures of a hydrated mantle wedge from antigorite crystal-preferred orientation (CPO). Earth Planet Sci Lett 375:395–407. https://doi.org/10.1016/j.epsl.2013.06.003

Bunge HJ (1982) Texture analysis in materials science—mathematical methods. Butterworths, London, p 593

Burdette E, Hirth G (2022) Creep rheology of antigorite: experiments at subduction zone conditions. J Geophys Res 127(7):e2022JB024260. https://doi.org/10.1029/2022JB024260

Burkhard DJM, O'Neill JR (1988) Contrasting serpentinization processes in the eastern Central Alps. Contr Mineral Petrol 99:498–506

Caglioti G, Paoletti A, Ricci FP (1958) Choice of collimators for a crystal spectrometer for neutron diffraction. Nucl Instrum 3:223–228. https://doi.org/10.1016/0369-643X(58)90029-X

Cannao E, Tiepolo M, Fumagalli P, Grieco G, Agostini S (2022) Metasomatism in the Finero phlogopite peridotite: new insights from C and N concentrations and d13C–d11B signatures. Chem Geol 614:121181. https://doi.org/10.1016/j.chemgeo.2022.121181

Capitani GC, Mellini M (2004) The modulated crystal structure of antigorite: the m=17 polysome. Am Mineral 89:147–148. https://doi.org/10.2138/am-2004-0117

Capitani GC, Mellini M (2006) The crystal structure of a second antigorite polysome (m=16), by single-crystal synchrotron diffraction. Am Mineral 91:394–399. https://doi.org/10.2138/am.2006.1919

Capitani G, Stixrude L, Mellini M (2009) First-principles energetics and structural relaxation of antigorite. Am Mineral 94:1271–1278. https://doi.org/10.2138/am.2009.3218

Caruso LJ, Chernosky JV (1979) The stability of lizardite. Can Mineral 17:757–770

Chernak LJ, Hirth G (2010) Deformation of antigorite serpentinite at high temperature and pressure. Earth Planet Sci Let 296:23–33. https://doi.org/10.1016/j.epsl.2010.04.035

Chernosky JV, Berman RG, Bryndzia LT (1988) Serpentine and chlorite equilibria. In: Bailey SW (ed) Hydrous phyllosilicates other than micas: Mineral. Soc. Am., reviews in mineralogy, vol 19, pp 295–346

Christensen NI (2004) Serpentine, peridotites and seismology. Int Geol Rev 46:795–816. https://doi.org/10.2747/0020-6814.46.9.795

Cisneros M, Behr WM, Platt JP, Anczkiewicz R (2022) Quartz-in-garnet barometry constraints on formation pressures of eclogites from the Franciscan Complex, California. Cont Mineral Petrol 177(12):1–23. https://doi.org/10.1007/s00410-021-01876-4

Clément M, Padrón-Navarta JA, Tommasi A (2019) Interplay between fluid extraction mechanisms and antigorite dehydration reactions (Val Malenco, Italian Alps). J Petrol 60:1935–1962. https://doi.org/10.1093/petrology/egz058

Cogulu E, Laurent R (1984) Mineralogical and chemical variations in chrysotile veins and peridotite host-rocks from the asbestos belt of southern Quebec. Can Mineral 22:173–183

Coleman RG (1971) Petrologic and geophysical nature of serpentinization. Geol Soc Am Bull 82:918–987. https://doi.org/10.1130/0016-7606(1971)82[897:PAGNOS]2.0.CO;2

Compagnoni R, Cossio R, Mellini M (2021) Raman anisotropy in serpentine minerals, with a caveat on identification. Raman Spectrosc 52:1334–1345. https://doi.org/10.1002/jrs.6128

Cooper WC, Murchio J, Popendorf W, Wenk H-R (1979) Chrysotile asbestos in a California recreational area. Science 206(4419):685–688. https://doi.org/10.1126/science.493972

Day HW, Chernosky JV, Kumin HJ (1985) Equilibria in the system MgO–SiO_2–H_2O: a thermodynamic analysis. Am Mineral 70:237–248

De Hoog JCM, Janak M, Vrabek M, Froitzheim N (2009) Serpentinized peridotites from an ultrahigh-pressure terrane in the Pohorje Mts. (Eastern Alps, Slovenia): geochemical constraints on petrogenesis and tectonic setting. Lithos 109:209–222. https://doi.org/10.1016/j.lithos.2008.05.006

Debret B, Andreani M, Godard M (2024) A review of abyssal serpentinite geochemistry and geodynamics. Earth-Sci Rev 258:104910. https://doi.org/10.1016/j.earscirev.2024.104910

Deng X, Luo C, Wentzcowitch RM, Aberg's GA, Wu Z (2022) Elastic anisotropy of lizardite at subduction zone conditions. Geophys Res Lett 49:e2022GL099712. https://doi.org/10.1029/2022gl099712

Díaz J, Gallart J, Ruiz M, Pulgar JA, López C, González-Cortina JM (2006) Probing seismic anisotropy in North Iberia from shear wave splitting. Phys Earth Planet Int 158:210–225. https://doi.org/10.1016/j.pepi.2005.12.011

Dietrich V, Peters TJ (1971) Regionale Verteilung der Mg-Phyllosilikate in den Serpentiniten des Oberhalbsteins. Schweiz Mineral Petrog Mitt 51:329–348

Díez Fernández R, Martínez Catalán JR, Arenas R, Abati J (2011) Tectonic evolution of a continental subduction-exhumation channel: Variscan structure of the basal allochthonous units in NW Spain. Tectonics 30:TC3009. https://doi.org/10.1029/2010TC002850

Dilissen N, Hidas K, Garrido CJ, Kahl W-A, Lopez-Sanchez-Vizcaino V, Padron-Navarta JA (2018) Textural evolution during high-pressure dehydration of serpentinite to peridotite and its relation to stress orientations and kinematics of subducting slabs: Insights from the Almirez ultramafic massif. Lithos 320–321:470–489. https://doi.org/10.1016/j.lithos.2018.09.033

Dodoni I, Buseck PR (2004) Serpentinites close-up and intimate: an HRTEM view. Int Geol Rev 46:507–527. https://doi.org/10.2747/0020-6814.46.6.507

Dodoni I, Posfal M, Buseck PR (2002) Revised structure models for antigorite: an HRTEM study. Am Mineral 87:1443–1458. https://doi.org/10.2138/am-2002-1022

Durand S, Juriček MP, Fischer KM (2024) Hydrous melting and its seismic signature. Elements 20:241–246. https://doi.org/10.2138/gselements.20.4.241

Ernst WG (1988) Tectonic history of subduction zones inferred from retrograde blueschist P-T paths. Geology 16(12):1081–1084. https://doi.org/10.1130/0091-7613(1988)016%3c1081:THOSZI%3e2.3.CO;2

Ernst WG (2011) Accretion of the Franciscan complex attending Jurassic-Cretaceous geotectonic development of northern and central California. Geol Soc Am Bull 123:1667–1678. https://doi.org/10.1130/B30398.1

Escartín J, Hirth G, Evans B (1997) Nondilatant brittle deformation of serpentinites: implications for Mohr–Coulomb theory and the strength of faults. J Geophys Res 102(B2):2897–2913. https://doi.org/10.1029/96JB02792

Evans BW (2004) The serpentinite multisystem revisited: chrysotile is metastable. Int Geol Rev 46:479–506. https://doi.org/10.2747/0020-6814.46.6.479

Evans BW (2010) Lizardite versus antigorite serpentinite: magnetite, hydrogen, and life? Geology 38(10):879–882. https://doi.org/10.1130/G31158.1

Evans BW, Johannes W, Oterdoom H, Trommsdorff V (1976) Stability of chrysotile and antigorite in the serpentinite multisystem. Schweiz Mineral Petrog Mitt 56:79–93

Evans BW, Hattori K, Baronnet A (2013) Serpentinite: what, why, where? Elements 9:99–106. https://doi.org/10.2113/gselements.9.2.99

Falini G, Foresti E, Gazzano M, Gualtieri AF, Leoni M, Lesci IG, Roveri N (2004) Tubular-shaped stoichiometric chrysotile nanocrystals. Chemistry 10:3043–3049. https://doi.org/10.1002/chem.200305685

Francis GH (1956) The serpentine mass in Glen Urquhart, Invernessshire, Scotland. Am J Sci 254(4):201–226

Frost BR, Beard JS (2007) On silica activity and serpentinization. J Petrol 48(7):1351–1368. https://doi.org/10.1093/petrology/egm021

Gatta C, Kantor I, Ballaran TB, Dubrovinsky L, McCammon C (2007) Effect of non-hydrostatic conditions on the elastic behaviour of magnetite: an in situ single-crystal X-ray diffraction study. Phys Chem Mineral 34:627–635. https://doi.org/10.1007/s00269-007-0177-3

Girardeau J, Gil Ibarguchi JI, Ben Jamaa N (1989) Evidence for heterogeneous upper mantle in the Cabo Ortegal Complex, Spain. Science 245:1231–1233. https://doi.org/10.1126/science.245.4923.1231

Gross P, Handy MR, John T, Pestal G, Pleuger J (2020) Crustal-scale sheath folding at HP conditions in an exhumed alpine subduction zone (Tauern Window, Eastern Alps). Tectonics 39:e2019TC005942. https://doi.org/10.1029/2019TC005942

Gualtieri A, Giacobbe C, Viti C (2012) The dehyroxylation of serpentine group minerals. Am Mineral 97:666–680. https://doi.org/10.2138/am.2012.3952

Guillot S, Schwartz S, Hattori KH, Auzende AL, Lardeaux JM (2004) The Monviso ophiolitic massif (Western Alps), a section through a serpentinite subduction channel. J Virtual Expl 16:1–17. https://doi.org/10.3809/jvirtex.2004.00099

Guillot S, Schwartz S, Reynard B, Agard P, Prigent C (2015) Tectonic significance of serpentinites. Rev Tectonophys 646:1–19. https://doi.org/10.1016/j.tecto.2015.01.0

Hartmann G, Wedepohl HK (1993) The composition of peridotite tectonites from the Ivrea complex, northern Italy: residues from melt extraction. Geochim Cosmochim Acta 57:1761–1782

Hazen RM, Finger LW (1989) High pressure crystal chemistry of andradite and pyrope: revised procedures for high-pressure diffraction experiments. Am Mineral 74:352–359

Hemley JJ, Montoya JW, Christ CL, Hostetler PB (1977) Mineral equilibria in the MgO–SiO_2–H_2O system. I. Talc-chrysotile-brucite stability relations. Am J Sci 277:322–351

Hermann J, Müntener O, Trommsdorff V, Hansmann W, Piccardo GB (1997) Fossil crust-to-mantle transition, Val Malenco (Italian Alps). J Geophys Res 102(B9):20123–20132. https://doi.org/10.1029/97JB01510

Hermann J, Müntener O, Scambelluri M (2000) The importance of serpentinite mylonites for subduction and exhumation of oceanic crust. Tectonophysics 327:225–238. https://doi.org/10.1016/S0040-1951(00)00171-2

Hilairet N, Daniel I, Reynard B (2006) Equation of state of antigorite, stability field of serpentines, and seismicity in subduction zones. Geophys Res Lett 33:L02302. https://doi.org/10.1029/2005gl024728

Hilairet N, Reynard B, Wang YB, Daniel I, Merkel S, Nishiyama N, Petitgirard S (2007) High-pressure creep of serpentine, interseismic deformation, and initiation of subduction. Science 318:1910–1913. https://doi.org/10.1126/science.1148494

Hirauchi K, Katayama I, Uehara S, Miyahara M, Takai Y (2010a) Inhibition of subduction thrust earthquakes by low-temperature plastic flow in serpentine. Earth Planet Sci Lett 295:349–357. https://doi.org/10.1016/j.epsl.2010.04.007

Hirauchi K, Michibayashi K, Ueda H, Katayama I (2010b) Spatial variations in antigorite fabric across a serpentinite subduction channel: insights from the Ohmachi Seamount, Izu-Bonin frontal arc. Earth Planet Sci Lett 229:196–206. https://doi.org/10.1016/j.epsl.2010.08.035

Hirose T, Bystricky M, Kunze K, Stunitz H (2006) Semi-brittle flow during dehydration of lizardite-chrysotile serpentinite deformed in torsion: implications for the rheology of oceanic lithosphere. Earth Planet Sci Let 249:484–493. https://doi.org/10.1016/j.epsl.2006.07.014

Jagodzinski H, Kunze G (1954) Die Röllchenstruktur des Chrysotils. I. Allgemeine Beugungstheorie und Kleinwinkelstreuung. Neues Jahrbuch für Mineralogie, Monatshefte, pp 95–108

Ji S, Li A, Wang Q, Long C, Wang H, Marcotte D, Salisbury M (2013) Seismic velocities, anisotropy, and shear-wave splitting of antigorite serpentinites and tectonic implications for subduction zones. J Geophys Res 118:1015–1037. https://doi.org/10.1002/jgrb.50110

Jung H (2011) Seismic anisotropy produced by serpentine in mantle wedge. Earth Planet Sci Lett 307:535–543. https://doi.org/10.1016/j.epsl.2011.05.041

Jung H, Green HW (2004) Experimental faulting of serpentinite during dehydration: implications for earthquakes, seismic low-velocity zones, and anomalous hypocenter distributions in subduction zones. Int Geol Rev 46(12):1089–1102. https://doi.org/10.2747/0020-6814.46.12.1089

Jung H, Fei YW, Silver PG, Green HW (2009) Frictional sliding in serpentine at very high pressure. Earth Planet Sci Lett 277:273–279. https://doi.org/10.1016/j.epsl.2017.06.016

Kashima A, Urashima S-h, Yui H (2022) Identifying the polymorphs of serpentine with micro-Raman spectroscopy: clear separation in biaxial plots. Raman Spec 53:1312–1320. https://doi.org/10.1002/jrs.6355

Katayama I, Hirauchi K, Michibayashi K, Ando J (2009) Trench-parallel anisotropy produced by serpentine deformation in the hydrated mantle wedge. Nature 461:1114–1117. https://doi.org/10.1038/nature08513

Kelley DS, Karson JA, Früh-Green G, Yoerger DR, Shank TM, Butterfield DA, Hayes JM, Schrenk MO, Olson EJ, Proskurowski G, Jakuba M, Bradley A, Larson B, Ludwig K, Glickson D, Buckman K, Bradley AS, Brazelton WJ, Roe K, Elend MJ, Delacour A, Bernasconi SM, Lilley MD, Baross JA, Summons RE, Sylva SP (2005) A serpentinite-hosted ecosystem: the lost city hydrothermal field. Science 307:1428–1434. https://doi.org/10.1126/science.1102556

Kempf ED, Hermann J, Connolly JAD (2022) Serpentinite dehydration at low pressure. Swiss J Geosci 115(14):1–30. https://doi.org/10.1186/s00015-022-00415-y

Kern H, Liu B, Popp T (1997) Relationship between anisotropy of P and S wave velocities and anisotropy of attenuation in serpentinite and amphibolite. J Geophys Res 102(B2):3051–3065. https://doi.org/10.1029/96JB03392

Kern H, Lokajicek T, Svitek T, Wenk H-R (2015) Seismic anisotropy of serpentinite from Val Malenco, Italy. J Geophys Res Solid Earth 120:4113–4129. https://doi.org/10.1002/2015JB012030

Kröner E (1958) Berechnung der elastischen Konstanten des Vielkristalls aus den Konstanten des Einkristalls. Zeitschr Phys 151:504–518

Kuehn R, Behrmann JH, Stipp M, Kilian R, Leiss B (2021) Deformation, CPO, and elastic anisotropy in low-grade metamorphic serpentinites, Atlantis Massif oceanic core complex. Geophys Res Lett 48:e2021GL092986. https://doi.org/10.1029/2021GL092986

Kunze G (1956) Die gewellte Struktur des Antigorits, I. Z Kristallogr 108:82–107

Lafay R, Baumgartner LP, Delacour A (2022) Preservation of mantle heterogeneities and serpentinization signature during antigorite dehydration: the example of the Bergell contact aureole. J Metamorph Geol 41:377–399. https://doi.org/10.1111/jmg.12699

Langer AM, Mackler AD, Pooley FD (1974) Electron microscopical investigation of asbestos fibers. Environ Health Persp 9:63–80

Laurora A, Brigatti MF, Malferrari D, Galli E, Rossi A, Ferrari M (2011) The crystal chemistry of lizardite-1T from north Apennines ophiolites near Modena, Italy. Can Mineral 49(4):1045–1054. https://doi.org/10.3749/canmin.49.4.1045

Lefeuvre N, Truche L, Donzé F-V, Ducoux M, Barré G, Fakoury R-A, Calassou S, Gaucher EC (2021) Native H_2 exploration in the Western Pyrenean Foothills. Geochem Geophys Geosyst 22(8):e2021GC009917. https://doi.org/10.1029/2021GC009917

Liu L (1986) Phase transformations in serpentine at high pressures and temperatures and implications for subducting lithosphere. Phys Earth Planet Int 42:255–262. https://doi.org/10.1016/0031-9201(86)90028-2

Liu W, Zhang J, Cao Y, Jin Z (2020) Geneses of two contrasting antigorite crystal preferred orientations and their implications for seismic anisotropy in the forearc mantle. J Geophys Res Solid Earth 125:1–24. https://doi.org/10.1029/2020JB019354

Long MD, Becker TW (2010) Mantle dynamics and seismic anisotropy. Earth Planet Sci Lett 297:341–354. https://doi.org/10.1016/j.epsl.2010.06.036

Lutterotti L, Matthies S, Wenk H-R, Schultz AJ, Richardson JW (1997) Combined texture and structure analysis of deformed limestone from time-of-flight neutron diffraction spectra. J Appl Phys 81:594–600. https://doi.org/10.1063/1.364220

Lutterotti L, Voltolini M, Wenk H-R, Bandyopadhyay K, Vanorio T (2010) Texture analysis of turbostratically disordered Ca-montmorillonite. Am Mineral 95:98–103. https://doi.org/10.2138/am.2010.3238

Lutterotti L, Vasin R, Wenk H-R (2014) Rietveld texture analysis from synchrotron diffraction images. I. Calibration and basic analysis. Powder Diffract 29:76–84. https://doi.org/10.1017/S0885715613001346

Matthies S (2010) On the combination of self-consistent and geometric mean elements for the calculation of the elastic properties of textured multi-phase samples. Solid State Phenom 160:87–93. https://doi.org/10.4028/www.scientific.net/SSP.160.87

Matthies S (2012) GEO-MIX-SELF calculations of the elastic properties of a textured graphite sample at different hydrostatic pressures. J Appl Cryst 45:1–16. https://doi.org/10.1107/S00218898 1104338X

Matthies S, Humbert M (1995) On the principle of a geometric mean of even-rank symmetric tensors for textured polycrystals. J Appl Cryst 28:254–266. https://doi.org/10.1107/S0021889894009623

Matthies S, Vinel GW (1982) On the reproduction of the orientation distribution function of texturized samples from reduced pole figures using the concept of a conditional ghost correction. Phys Stat Solidi (b) 112:K111-114

Matthies S, Wenk H-R (2009) Transformations for monoclinic crystal symmetry in texture analysis. J Appl Cryst 42:564–571. https://doi.org/10.1107/S0021889809018172

Matthies S, Priesmeyer HG, Daymond MR (2001) On the diffractive determination of single-crystal elastic constants using polycrystalline samples. J Appl Cryst 34:585–601. https://doi.org/10.1107/S0021889801010482

Mellini M (1982) The crystal structure of lizardite 1T: hydrogen bonds and polytypism. Am Mineral 67:587–598

Mellini M, Viti C (1994) Crystal structure of lizardite-1T from Elba, Italy. Am Mineral 79:1194–1198

Mellini M, Zanazzi PF (1987) Crystal structures of lizardite-1T and lizardite-2H1 from Coli, Italy. Am Mineral 72:943–948

Mellini M, Trommsdorff V, Compagnoni R (1987) Antigorite polysomatism: behaviour during progressive metamorphism. Contrib Mineral Petrol 97:147–155

Melosh BL (2019) Fault initiation in serpentinite. Geochem Geophys Geosyst 20:2626–2646. https://doi.org/10.1029/2018GC008092

Michibayashi K, Mainprice D (2004) The role of pre-existing mechanical anisotropy on shear zone development within oceanic mantle lithosphere: an example from the Oman Ophiolite. J Petrol 45(2):405–414. https://doi.org/10.1093/petrology/egg099

Montgomery DR (1993) Compressional uplift in the central California coast ranges. Geology 21(6):543–546

Moody JB (1976) An experimental study on the serpentinization of iron-bearing olivines. Can Mineral 14:462–478

Mookherjee M, Mainprice D (2014) Unusually large shear wave anisotropy for chlorite in subduction zone settings. Geophys Res Lett 41(5):1506–1513. https://doi.org/10.1002/2014GL059334

Mookherjee M, Stixrude L (2009) Structure and elasticity of serpentine at high-pressure. Earth Planet Sci Lett 279:11–19. https://doi.org/10.1016/j.epsl.2008.12.018

Moore DE, Rymer MJ (2007) Talc-bearing serpentinite and the creeping section of the San Andreas fault. Nature 448:795–797. https://doi.org/10.1038/nature06064

Moores EM (1970) Ultramafics and orogeny, with models of the U.S. Cordillera and the Tethys. Nature 228:837–842

Morales LFG, Mainprice D, Kern H (2018) Olivine-antigorite orientation relationships: microstructures, phase boundary misorientations and the effect of cracks in the seismic properties of serpentinites. Tectonophysics 724–725:93–115. https://doi.org/10.1016/j.tecto.2017.12.009

Mumpton FA, Thompson CS (1975) Mineralogy and origin of the Coalinga asbestos deposit. Clays Clay Miner 23:131–143

Müntener O, Hermann J (1994) Titanian andradite in a metapyroxenite layer from the Malenco ultramafics (Italy): implications for Ti-mobility and low oxygen fugacity. Contrib Miner Petrol 116:156–168

Müntener O, Hermann J (1996) The Val Malenco lower crust-upper mantle complex and its field relations (Italian Alps). Schweiz Mineral Petrogr Mitt 76:475–500

Müntener O, Hermann J, Trommsdorff V (2000) Cooling history and exhumation of lower crustal granulites and upper mantle (Malenco Eastern Central Alps). J Petrol 41:175–200. https://doi.org/10.1093/petrology/41.2.175

Müntener O, Manatschal G, Desmurs L, Pettke T (2010) Plagioclase peridotites in ocean–continent transitions: refertilized mantle domains generated by melt stagnation in the shallow mantle lithosphere. J Petrol 51(1–2):255–294. https://doi.org/10.1093/petrology/egp087

Nagaya T, Wallis SR, Seto Y, Miyake A, Soda Y, Uehara S, Matsumoto M (2017) Minimizing and quantifying mis-indexing in electron backscatter diffraction (EBSD) determinations of antigorite crystal directions. J Struct Geol 95:127–141. https://doi.org/10.1016/j.jsg.2016.12.006

Nespereira J, Navarro R, Monterrubio S, Yenes M (2019) Serpentinite from Moeche (Galicia, North Western Spain). A stone used for centuries in the construction of the architectural heritage of the region. Sustainability 11:2700. https://doi.org/10.3390/su11092700

Nestola F, Angel R, Zhao J, Garrido C, López Sanchez-Vizcaıno V, Capitani G, Mellini M (2010) Antigorite equation of state and anomalous softening at 6 GPa: an in situ single-crystal X-ray diffraction study. Contrib Mineral Petrol 160:33–43. https://doi.org/10.1007/S00410-009-0463-9

Nishi M, Irifune T, Tsuchiya J, Tange Y, Nishihara Y, Fujino K, Higo Y (2014) Stability of hydrous silicate at high pressures and water transport to the deep lower mantle. Nat Geo 7:224–227. https://doi.org/10.1038/ngeo2074

Nishii A, Wallis SR, Mizukami T, Michibayashi K (2011) Subduction related antigorite CPO patterns from forearc mantle in the Sanbagawa belt, southwest Japan. J Struct Geol 33:1436–1445. https://doi.org/10.1016/j.jsg.2011.08.006

Nye JF (1985) The physical properties of crystals: their representation by tensors and matrices. Oxford University Press, Oxford, p 330

O'Hanley DS (1996) Serpentinites: records of tectonic and petrologic history. Oxford University Press, Oxford, UK, p 277

O'Hanley DS, Chernosky JV Jr, Wicks JF (1989) The stability of lizardite and chrysotile. Canad Mineral 27:483–494

Ohira I, Ohtani E, Sakai T, Miyahara M, Hirao N, Ohishi Y, Nishijima M (2014) Stability of a hydrous δ-phase, AlOOH-$MgSi_2(OH)_2$, and a mechanism for water transport into the base of the lower mantle. Earth Planet Sci Lett 401:12–17. https://doi.org/10.1016/j.epsl.2014.05.059

Ordóñez Casado B, Gebauer D, Schäfer HJ, Gil Ibarguchi JI, Peucat JJ (2001) A single Devonian subduction event for the HP/HT metamorphism of the Cabo Ortegal complex within the Iberian Massif. Tectonophysics 332:359–385. https://doi.org/10.1016/S0040-1951(00)00210-9

Otten MT (1993) High-resolution transmission electron-microscopy of polysomatism and stacking defects in antigorite. Am Mineral 78:75–84

Padrón-Navarta JA, Hermann J, Garrido CJ, Sánchez-Vizcaıno VL, Gomez-Pugnaire MT (2010) An experimental investigation of antigorite dehydration in natural silica-enriched serpentinite. Contrib Mineral Petrol 159:25–42. https://doi.org/10.1007/s00410-009-0414-5

Padrón-Navarta JA, Tommasi A, Garrido CJ, Sánchez-Vizcaino VL (2012) Plastic deformation and development of antigorite preferred orientation in high pressure serpentinites. Earth Planet Sci Lett 349–350(2):75–86. https://doi.org/10.1016/j.epsl.2012.06.049

Padrón-Navarta JA, Sánchez-Vizcaíno VL, Hermann J, Connolly JAD, Garrido CJ, Gómez-Pugnaire MT, Marchesi C (2013) Tschermak's substitution in antigorite and consequences for phase relations and water liberation in high-grade serpentinites. Lithos 178:186–196. https://doi.org/10.1016/J.LITHOS.2013.02.001

Page NJ (1968) Chemical differences among the serpentine "polymorphs." Am Mineral 53:201–215

Park J, Yuan H, Levin V (2004) Subduction zone anisotropy beneath Corvallis, Oregon: a serpentinite skid mark of trench-parallel terrane migration? J Geophys Res 109:B10306. https://doi.org/10.1029/2003JB002718

Paterson SR, Wainger L (1991) Strains and structures associated with a terraine bounding stretching fault: the Melones fault zone, central Sierra Nevada, California. Tectonophysics 194(1–2):69–90

Perdew JP, Burke K, Ernzerhof M (1996) Generalized gradient approximation made simple. Phys Rev Lett 77(18):3865–3868

Peretti A, Dubessy J, Mullis J, Frost BR, Trommsdorff V (1992) Highly reducing conditions during Alpine metamorphism of the Malenco peridotite (Sondrio, northern Italy) indicated by mineral paragenesis and H_2 in fluid inclusions. Cont Mineral Petrol 112:329–340

Pollastri S, Perchiazzi N, Lezzerini M, Plaisier JR, Cavallo A, Dalconi MC, Gandolfi NB, Gualtieri AF (2016) The crystal structure of mineral fibres, 1. Chrysotile. Period Mineral 85:249–259. https://doi.org/10.2451/2016PM655

Popa NC (1998) The (hkl) dependence of diffraction-line broadening caused by strain and size for all Laue groups in Rietveld refinement. J Appl Cryst 31:176–180. https://doi.org/10.1107/S0021889897009795

Rakovan J (2011) Word to the wise: serpentine, California's state rock. Rocks Minerals 86:63–68. https://doi.org/10.1080/00357529.2011.537187

Raleigh CB, Paterson MS (1965) Experimental deformation of serpentinite and its tectonic implications. J Geophys Res 70(16):3965–3985. https://doi.org/10.1029/JZ070i016p03965

Ranero CR, Pérez-Gussinyé M (2010) Sequential faulting explains the asymmetry and extension discrepancy of conjugate margins. Nature 468:294–299. https://doi.org/10.1038/nature09520

Reuss A (1929) Berechnung der Fließgrenze von Mischkristallen auf Grund der Plastizitätsbedingung für Einkristalle. Z Angew Math Mech 9:49–58

Rietveld HM (1969) A profile refinement method for nuclear and magnetic structures. J Appl Cryst 2:65–71. https://doi.org/10.1107/S0021889869006558

Rinaudo C, Gastaldi D, Belluso E (2003) Characterization of chrysotile, antigorite and lizardite by FT-Raman spectroscopy. Can Mineral 41:883–890. https://doi.org/10.2113/gscanmin.41.4.883

Ringwood AE, Major A (1967) High-pressure reconnaissance investigations in the system Mg_2SiO_4-MgO-H_2O. Earth Planet Sci Lett 2(2):130–133. https://doi.org/10.1016/0012-821X(67)90114-8

Rooney JS, Tarling MS, Smith SAF, Gordon KC (2018) Submicron Raman spectroscopy mapping of serpentinite fault rocks. J Raman Spectros 49:279–286. https://doi.org/10.1002/jrs.5277

Rosa A, Sanchez-Valle C, Nisr C, Evans S, Debord R, Merkel S (2013) Shear wave anisotropy in textured phase d and constraints on deep water recycling in subduction zones. Earth Planet Sci Lett 377–378:13–22. https://doi.org/10.1016/j.epsl.2013.06.036

Ruiz M, Diaz J, Pedreira D, Gallart J, Pulgar JA (2017) Crustal structure of the North Iberian continental margin from seismic refraction/wide-angle reflection profiles. Tectonophysics 717:65–82. https://doi.org/10.1016/j.tecto.2017.07.008

Saleebe JB (1982) Polygenetic ophiolite belt of the California Sierra Nevada: geochronological and tectonostratigraphic development. J Geophys Res Solid Earth 87(B3):1735–1926. https://doi.org/10.1029/JB087iB03p01803

Sánchez Martínez S, Arenas R, Díaz García F, Martínez Catalán JR, Gómez-Barreiro J, Pearce JA (2007) Careón Ophiolite, NW Spain: supra-subduction zone setting for the youngest Rheic ocean floor. Geology 35:53–56. https://doi.org/10.1130/g23024a.1

Satta N, Morales LFG, Criniti G, Kurnosov A, Ballaran TB, Speziale S, Marquardt K, Capitani GC, Marquardt H (2022) Single-crystal elasticity of antigorite at high pressure and seismic detection of serpentinized slabs. Geophys Res Lett 49:e2022GL099411. https://doi.org/10.1029/2022GL099411

Schmid SM, Fügenschuh B, Kissling E, Schuster R (2004) Tectonic map and overall architecture of the Alpine orogen. Eclogae Geol Helv 97:93–117. https://doi.org/10.1007/s00015-004-1113-x

Schmid SM, Scharf A, Handy MR, Rosenberg CL (2013) The Tauern Window (Eastern Alps, Austria): a new tectonic map, with cross-sections and a tectonometamorphic synthesis. Swiss J Geosci 106(1):1–32. https://doi.org/10.1007/s00015-013-0123-y

Schmitt DR, Han Z, Kravchinsky VA, Escartin J (2007) Seismic and magnetic anisotropy of serpentinized ophiolite: implications for oceanic spreading rate dependent anisotropy. Earth Planet Sci Let 261:590–601. https://doi.org/10.1016/j.epsl.2007.07.024

Schmutz HU (1976) Der Mafitit-Ultramafitit-Komplex zwischen Chiavenna und Val Bondasca (Provinz Sondrio, Italien; Kt. Graubünden, Schweiz). Beitr Geol Karte Schweiz, Neue Folge 149, p 73

Schroeder T, John B, Frost BR (2002) Geologic implications of seawater circulation through peridotite exposed at slow-spreading mid-ocean ridges. Geology 30:367–370

Schwartz S, Guillot S, Reynard B, Lafay R, Debret B, Nicollet C, Lanari P, Auzende AL (2013) Pressure–temperature estimates of the lizardite/antigorite transition in high pressure serpentinites. Lithos 178:197–210. https://doi.org/10.1016/j.lithos.2012.11.023

Shao T, Ji S, Kondo Y, Michibayashi K, Wang Q, Xu Z, Sun S, Marcotte D, Salisbury MH (2014) Antigorite-induced seismic anisotropy and implications for deformation in subduction zones. J Geophys Res Solid Earth 119:2068–2099. https://doi.org/10.1002/2013JB010661

Shieh SR, Mao H-k, Hemley RJ, Ming LC (2000) In situ X-ray diffraction studies of dense hydrous magnesium silicates at mantle

conditions. Earth Planet Sci Lett 177:69–80. https://doi.org/10.1016/S0012-821X(00)00033-9
Soda Y, Takagi H (2010) Sequential deformation from serpentinite mylonite to metasomatic rocks along the Sashu Fault, SW Japan. J Struct Geol 32:792–802. https://doi.org/10.1016/j.jsg.2010.05.003
Soda Y, Wenk H-R (2014) Antigorite crystallographic preferred orientations in serpentinites from Japan. Tectonophysics 615–616:199–212. https://doi.org/10.1016/j.tecto.2013.12.016
Springer RK (1974) Contact metamorphosed ultramafic rocks in the Western Sierra Nevada Foothills, California. J Petrol 15(1):160–195
Tarling MS, Smith SAF, Scott JM (2019) Fluid overpressure from chemical reactions in serpentinite within the source region of deep episodic tremor. Nat Geosci 12:1034–1042
Tarling MS, Smith SAF, Rooney JS, Viti C, Gordon KC (2021) A common type of mineralogical banding in serpentine crack-seal veins. Earth Planet Sci Lett 564:116930. https://doi.org/10.1016/j.epsl.2021.116930
Trommsdorff V, Evans BW (1972) Progressive metamorphism of antigorite schist in the Bergell tonalite aureole (Italy). Am J Sci 272:423–437
Truche L, Donzé F-V, Goskolli E, Muceku B, Loisy C, Monnin C, Dutoit H, Cerepi A (2024) A deep reservoir for hydrogen drives intense degassing in the Bulqizë ophiolite. Science 383:618–621. https://doi.org/10.1126/science.adk9099
Uehara S, Shirozu H (1985) Variations in chemical composition and structural properties of antigorites. Mineral Mag 12:299–318
Ulian G, Moro D, Valdre G (2018) First principle investigation of the mechanical properties of natural layered nanocomposite: Clinochlore as a model system for heterodesmic structures. Compos Struct 202:551–558. https://doi.org/10.1016/j.compstruct.2018.02.089
Ulmer P, Trommsdorff V (1995) Serpentine stability to mantle depths and subduction-related magmatism. Science 268(5212):858–861
Van de Moortele B, Bezacier L, Trullenque G, Reynard B (2010) Electron back-scattering diffraction (EBSD) measurements of antigorite lattice-preferred orientations (LPO). J Microsc 239(3):245–248. https://doi.org/10.1111/j.1365-2818.2010.03398.x
Veblen DR, Buseck PR (1979) Serpentine minerals: intergrowths and new combination structures. Science 206:1398–1400
Viti C, Mellini M (1997) Contrasting chemical compositions in associated lizardite and chrysotile in veins from Elba, Italy. Eur J Mineral 9:585–596
Viti C, Mellini M (1998) Mesh textures and bastites in the Elba retrograde serpentinites. Eur J Mineral 10:1341–1359
Viti C, Collettini C, Tesei T, Tarling MS, Smith SAF (2018) Deformation processes, textural evolution and weakening in retrograde serpentinites. Minerals 8(6):241. https://doi.org/10.3390/min8060241
Voigt W (1887) Theoretische Studien über die Elastizitätsverhältnisse der Krystalle. Dieterichsche Verlags-Buchhandlung, Göttingen, p 100
Wakabayashi J (2004) Contrasting settings of serpentinite bodies, San Francisco Bay Area, California: derivation from the subducting plate vs. mantle hanging wall. Int Geol Rev 46:1103–1118. https://doi.org/10.2747/0020-6814.46.12.1103
Wakabayashi J (2017) Serpentinites and serpentinites: Variety of origins and emplacement mechanisms of serpentinite bodies in the California Cordillera. Island Arc 26:1–14. https://doi.org/10.1111/iar.12205
Wang Q, Bagdassarov N, Ji S (2013) The Moho as a transition zone: a revisit from seismic and electrical properties of minerals and rocks. Tectonophysics 609:395–422. https://doi.org/10.1016/j.tecto.2013.08.041
Wassmann S, Stöckhert B, Trepmann CA (2011) Dissolution precipitation creep versus crystalline plasticity in high-pressure metamorphic serpentinites. Geol Soc Lond Spec Publ 360:129–149. https://doi.org/10.1144/SP360.8
Watanabe T, Shirasugi Y, Yano H, Michibayashi K (2011) Seismic velocity in antigorite-bearing serpentinite mylonites. Geol Soc Lond Spec Publ 360:97–112. https://doi.org/10.1144/SP360.6
Watanabe T, Shirasugi Y, Michibayashi K (2014) A new method for calculating velocities in rocks containing strongly dimensionally anisotropic mineral grains and its application to antigorite-bearing serpentinite mylonites. Earth Planet Sci Lett 391:24–35. https://doi.org/10.1016/j.epsl.2014.01.025
Wenk H-R, Matthies S, Donovan J, Chateigner D (1998) BEARTEX: a windows-based program system for quantitative texture analysis. J Appl Cryst 31:262–269. https://doi.org/10.1107/S002188989700811X
Wenk H-R, Kanitpanyacharoen W, Voltolini M (2010) Preferred orientation of phyllosilicates: comparison of fault gouge, shale and schist. J Struct Geol 32:478–489. https://doi.org/10.1016/j.jsg.2010.02.003
Wenk H-R, Kanitpanyacharoen W, Ren Y (2019) Slate—a new record for crystal preferred orientation. J Struct Geol 125:319–324. https://doi.org/10.1016/j.jsg.2017.12.009
Wenk H-R, Yu R, Cardenes V, Lopez-Sanchez MA, Sintubin M (2020) Review: fabric and anisotropy of slates: from classical studies to new results. J Struct Geol 138:104066. https://doi.org/10.1016/j.jsg.2020.104066
Wenk H-R, Huang J, Devoe M, Gomez-Barreiro J, Vasin R, Ren Y, Barrios-Sanchez S (2022) Crystallographic and shape preferred orientation and anisotropy in slates from Northern Spain. J Struct Geol 164:104730. https://doi.org/10.1016/j.jsg.2022.104730
Whittaker E (1956) The structure of chrysotile. II. Clinochrysotile. Acta Cryst 9:855–862
Wicks FJ, Whittaker EJW (1977) Serpentine textures and serpentinization. Can Mineral 15:459–488
Wiens DA, Conder JA, Faul UH (2008) The seismic structure and dynamics of the mantle wedge. Ann Rev Earth Planet Sci 36:421–455. https://doi.org/10.1146/annurev.earth.33.092203.122633
Worden RH, Droop GTR, Champness PE (1991) The reaction antigorite ⇒ olivine + talc + H_2O in the Bergell aureole. N Italy Mineral Mag 55:367–377
Wu W, Nishihara Y, Tsujino N (2024) Crystallographic preferred orientation of phase D at high pressure and temperature: implications for seismic anisotropy in the mid-mantle. J Geophys Res Solid Earth 129(10):e2024JB029734. https://doi.org/10.1029/2024JB029734
Wunder B, Wirth R, Gottschalk M (2001) Antigorite: Pressure and temperature dependence of polysomatism and water content. Eur J Mineral 13:485–495. https://doi.org/10.1127/0935-1221/2001/0013-0485
Xu C, Greaux S, Inoue T, Noda M, Gao J, Li Y (2022) Sound velocities of superhydrous phase B up to 21 GPa and 900K. Geophys Res Lett 49:e2022GL098674. https://doi.org/10.1029/2022GL098674
Yada K (1971) Study of the microstructure of chrysotile asbestos by high resolution electron microscopy. Acta Cryst A 27:659–664
Yada K (1979) Microstructures of chrysotile and antigorite by high-resolution electron microscopy. Can Mineral 17:679–692
Yamasaki T, Seno T (2003) Double seismic zone and dehydration embrittlement of the subducting slab. J Geophys Res 108(B4):2212. https://doi.org/10.1029/2002JB001918
Yang H, Prewitt CT, Frost DJ (1997) Crystal structure of the dense hydrous magnesium silicate, phase D. Am Mineral 82:651–654. https://doi.org/10.2138/am-1997-5-627

Zanazzi PF, Montagnoli M, Nazzareni S, Comodi P (2007) Structural effects of pressure on monoclinic chlorite: a single crystal study. Am Mineral 92:655–661. https://doi.org/10.2138/am.2007.2341

Zhang H, Gilbert B, Banfield JF (2021) Atomic perspective on the serpentine-chlorite solid-state transformation. Chem Mater 33:6338–6345. https://doi.org/10.1021/acs.chemmater.1c00894

Zhao L, Malusà MG, Yuan H, Paul A, Guillot S, Lu Y, Stehly L, Solarino S, Eva E, Bodin LuG (2020) Evidence for a serpentinized plate interface favouring continental subduction. Nat Commun 11(1):1–8. https://doi.org/10.1038/s41467-020-15904-7

Zucali M, Marinoni N, Diella V, Croce A, Rinaudo C, Fontana E (2018) Deciphering the tectonic-geodynamic context of the gem-quality "noble serpentine" deposit formation combining microstructural, chemical and micro-Raman analyses in Palaeozoic olivine-bearing marbles and serpentine-hosting rocks (Pizzo Tremogge, Margna unit–Austroalpine, Val Malenco–Central Alps, Italy). Ore Geol Rev 92:257–270. https://doi.org/10.1016/j.oregeorev.2017.11.020